



MIT Open Access Articles

Combined analysis of all three phases of solar neutrino data from the Sudbury Neutrino Observatory

The MIT Faculty has made this article openly available. **Please share** how this access benefits you. Your story matters.

Citation	Aharmim, B., S. N. Ahmed, A. E. Anthony, N. Barros, E. W. Beier, A. Bellerive, B. Beltran, et al. "Combined analysis of all three phases of solar neutrino data from the Sudbury Neutrino Observatory." Physical Review C 88, no. 2 (August 2013). © 2013 American Physical Society
As Published	http://dx.doi.org/10.1103/PhysRevC.88.025501
Publisher	American Physical Society
Version	Final published version
Citable link	http://hdl.handle.net/1721.1/81363
Terms of Use	Article is made available in accordance with the publisher's policy and may be subject to US copyright law. Please refer to the publisher's site for terms of use.

Combined analysis of all three phases of solar neutrino data from the Sudbury Neutrino Observatory

B. Aharmim,⁶ S. N. Ahmed,¹⁴ A. E. Anthony,^{17,a} N. Barros,^{8,b} E. W. Beier,¹³ A. Bellerive,⁴ B. Beltran,¹ M. Bergevin,^{7,5,c} S. D. Biller,¹² K. Boudjemline,^{4,14} M. G. Boulay,¹⁴ B. Cai,¹⁴ Y. D. Chan,⁷ D. Chauhan,⁶ M. Chen,¹⁴ B. T. Cleveland,¹² G. A. Cox,^{19,d} X. Dai,^{14,12,4} H. Deng,¹³ J. A. Detwiler,⁷ M. DiMarco,¹⁴ P. J. Doe,¹⁹ G. Doucas,¹² P.-L. Drouin,⁴ F. A. Duncan,^{16,14} M. Dunford,^{13,e} E. D. Earle,¹⁴ S. R. Elliott,^{9,19} H. C. Evans,¹⁴ G. T. Ewan,¹⁴ J. Farine,^{6,4} H. Fergani,¹² F. Fleurot,⁶ R. J. Ford,^{16,14} J. A. Formaggio,^{11,19} N. Gagnon,^{19,9,7,12} J. TM. Goon,¹⁰ K. Graham,^{4,14} E. Guillian,¹⁴ S. Habib,¹ R. L. Hahn,³ A. L. Hallin,¹ E. D. Hallman,⁶ P. J. Harvey,¹⁴ R. Hazama,^{19,f} W. J. Heintzelman,¹³ J. Heise,^{2,9,14,g} R. L. Helmer,¹⁸ A. Hime,⁹ C. Howard,^{1,h} M. Huang,^{17,6,i} P. Jagam,⁵ B. Jamieson,² N. A. Jelley,¹² M. Jerkins,¹⁷ K. J. Keeter,^{14,j} J. R. Klein,^{17,13} L. L. Kormos,^{14,k} M. Kos,¹⁴ C. Kraus,^{14,6} C. B. Krauss,¹ A. Kruger,⁶ T. Kutter,¹⁰ C. C. M. Kyba,^{13,l} R. Lange,³ J. Law,⁵ I. T. Lawson,^{16,5} K. T. Lesko,⁷ J. R. Leslie,¹⁴ J. C. Loach,^{12,7} R. MacLellan,^{14,m} S. Majerus,¹² H. B. Mak,¹⁴ J. Maneira,⁸ R. Martin,^{14,7} N. McCauley,^{13,12,n} A. B. McDonald,¹⁴ S. R. McGee,¹⁹ M. L. Miller,^{11,o} B. Monreal,^{11,p} J. Monroe,^{11,q} B. G. Nickel,⁵ A. J. Noble,^{14,4} H. M. O'Keeffe,¹² N. S. Oblath,^{19,11} R. W. Ollerhead,⁵ G. D. Orebi Gann,^{12,13,r} S. M. Oser,² R. A. Ott,¹¹ S. J. M. Peeters,^{12,s} A. W. P. Poon,⁷ G. Prior,^{7,e} S. D. Reitzner,⁵ K. Rielage,^{9,19} B. C. Robertson,¹⁴ R. G. H. Robertson,¹⁹ R. C. Rosten,¹⁹ M. H. Schwendener,⁶ J. A. Secrest,^{13,t} S. R. Seibert,^{17,9,13} O. Simard,^{4,u} J. J. Simpson,⁵ P. Skensved,¹⁴ T. J. Sonley,^{11,v} L. C. Stonehill,^{9,19} G. Tešić,^{4,w} N. Tolich,¹⁹ T. Tsui,² R. Van Berg,¹³ B. A. VanDevender,^{19,x} C. J. Virtue,⁶ H. Wan Chan Tseung,^{12,19} D. L. Wark,^{15,y} P. J. S. Watson,⁴ J. Wendland,² N. West,¹² J. F. Wilkerson,^{19,h} J. R. Wilson,^{12,z} J. M. Wouters,^{9,aa} A. Wright,^{14,bb} M. Yeh,³ F. Zhang,⁴ and K. Zuber^{12,b}
(SNO Collaboration)

¹Department of Physics, University of Alberta, Edmonton, Alberta T6G 2R3, Canada

²Department of Physics and Astronomy, University of British Columbia, Vancouver BC V6T 1Z1, Canada

³Chemistry Department, Brookhaven National Laboratory, Upton, New York 11973-5000, USA

⁴Ottawa-Carleton Institute for Physics, Department of Physics, Carleton University, Ottawa, Ontario K1S 5B6, Canada

⁵Physics Department, University of Guelph, Guelph, Ontario N1G 2W1, Canada

⁶Department of Physics and Astronomy, Laurentian University, Sudbury, Ontario P3E 2C6, Canada

⁷Institute for Nuclear and Particle Astrophysics and Nuclear Science Division, Lawrence Berkeley National Laboratory, Berkeley, California 94720, USA

⁸Laboratório de Instrumentação e Física Experimental de Partículas, Av. Elias Garcia 14, 1º, 1000-149 Lisboa, Portugal

⁹Los Alamos National Laboratory, Los Alamos, New Mexico 87545, USA

¹⁰Department of Physics and Astronomy, Louisiana State University, Baton Rouge, Louisiana 70803, USA

¹¹Laboratory for Nuclear Science, Massachusetts Institute of Technology, Cambridge, Massachusetts 02139, USA

¹²Department of Physics, University of Oxford, Denys Wilkinson Building, Keble Road, Oxford OX1 3RH, United Kingdom

¹³Department of Physics and Astronomy, University of Pennsylvania, Philadelphia, Pennsylvania 19104-6396, USA

¹⁴Department of Physics, Queen's University, Kingston, Ontario K7L 3N6, Canada

¹⁵Rutherford Appleton Laboratory, Chilton, Didcot OX11 0QX, United Kingdom

¹⁶SNOLAB, Sudbury, Ontario P3Y 1M3, Canada

¹⁷Department of Physics, University of Texas at Austin, Austin, Texas 78712-0264, USA

¹⁸TRIUMF, 4004 Wesbrook Mall, Vancouver BC V6T 2A3, Canada

¹⁹Center for Experimental Nuclear Physics and Astrophysics, and Department of Physics, University of Washington, Seattle, Washington 98195, USA

(Received 14 September 2011; revised manuscript received 28 May 2013; published 1 August 2013)

We report results from a combined analysis of solar neutrino data from all phases of the Sudbury Neutrino Observatory (SNO). By exploiting particle identification information obtained from the proportional counters installed during the third phase, this analysis improved background rejection in that phase of the experiment. The combined analysis of the SNO data resulted in a total flux of active neutrino flavors from ^8B decays in the Sun of $(5.25 \pm 0.16(\text{stat.})_{-0.13}^{+0.11}(\text{syst.})) \times 10^6 \text{ cm}^{-2} \text{ s}^{-1}$, while a two-flavor neutrino oscillation analysis yielded $\Delta m_{21}^2 = (5.6_{-1.4}^{+1.9}) \times 10^{-5} \text{ eV}^2$ and $\tan^2 \theta_{12} = 0.427_{-0.029}^{+0.033}$. A three-flavor neutrino oscillation analysis combining the SNO result with results of all other solar neutrino experiments and reactor neutrino experiments yielded $\Delta m_{21}^2 = (7.46_{-0.19}^{+0.20}) \times 10^{-5} \text{ eV}^2$, $\tan^2 \theta_{12} = 0.443_{-0.025}^{+0.030}$, and $\sin^2 \theta_{13} = (2.49_{-0.32}^{+0.20}) \times 10^{-2}$.

DOI: 10.1103/PhysRevC.88.025501

PACS number(s): 26.65.+t, 14.60.Pq, 13.15.+g, 95.85.Ry

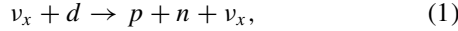
I. INTRODUCTION

The Sudbury Neutrino Observatory (SNO) was designed to measure the flux of neutrinos produced by ^8B decays in the Sun, so-called ^8B neutrinos, and to study neutrino oscillations,

as proposed by Chen [1]. As a result of measurements with the SNO detector and other experiments, it is now well established that neutrinos are massive and that the weak eigenstates (ν_e , ν_μ , ν_τ) are mixtures of the mass eigenstates (ν_1 , ν_2 , ν_3).

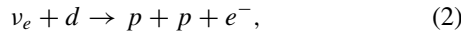
The probability of detecting a neutrino in the same weak eigenstate in which it was created depends on the energy and propagation distance of the neutrino, the effects of matter [2,3], the neutrino mixing angles (θ_{12} , θ_{23} , θ_{13}), a phase (δ) which can lead to charge-parity violation, and the differences between the squares of the neutrino mass eigenvalues (Δm_{21}^2 , Δm_{32}^2 , Δm_{31}^2) [4,5].

The SNO detector observed ^8B neutrinos via three different reactions. By measuring the rate of neutral current (NC) reactions,



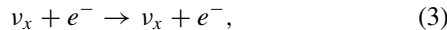
which is equally sensitive to all three active neutrino flavors, the SNO experiment determined the total active ^8B neutrino flux, Φ_B , independently of any specific active neutrino flavor oscillation hypothesis [1]. The predicted flux from solar model calculations [6] is $(5.88 \pm 0.65) \times 10^6 \text{ cm}^{-2}\text{s}^{-1}$, BPS09(GS), or $(4.85 \pm 0.58) \times 10^6 \text{ cm}^{-2}\text{s}^{-1}$, BPS09(AGSS09), using a recent measurement of the heavy-element abundance at the Sun's surface. Previous analyses of SNO data [7,8] measured Φ_B more precisely than the solar model predictions. A more precise measurement of Φ_B would better constrain these solar models, but may not necessarily determine which metallicity is correct due to the large uncertainties at present on both predictions.

By measuring the rate of charged current (CC) reactions,



which is only sensitive to ν_e s, and comparing this to the NC reaction rate, it was possible to determine the neutrino survival probability as a function of energy. This can then constrain the neutrino oscillation parameters independently of any specific prediction of Φ_B .

The SNO experiment also measured the rate of elastic scattering (ES) reactions,



which is sensitive to all neutrino flavors, but the cross section for ν_e s is approximately six times larger than that for the other flavors.

We present in this article a final combined analysis of all solar neutrino data from the SNO experiment including a new technique for the analysis of the data from the third phase and an improved analysis of the data from the first two phases. Section II gives an overview of the detector. In Sec. III we describe the method used to combine all the data in a fit which determines Φ_B and a parametrized form of the ν_e survival probability. Section IV describes a new particle identification technique that allowed us to significantly suppress the background events in the proportional counters used in the third phase of the SNO experiment. Section V presents the results of the new analysis of data from Phase III, and the combined analysis of data from all phases. The results of this combined analysis are interpreted in the context of neutrino oscillations in Sec. VI.

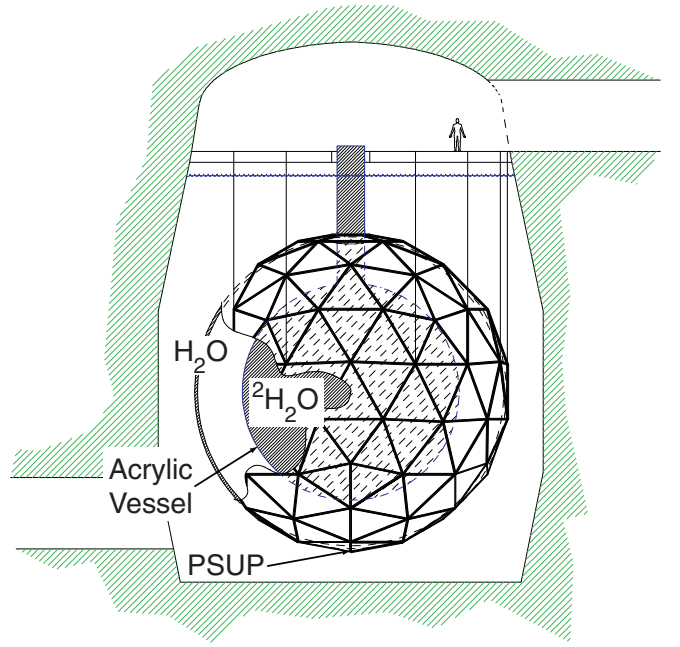


FIG. 1. (Color online) Schematic diagram of the SNO detector. We used a coordinate system with the center of the detector as the origin, and z direction as vertically upward.

II. THE SNO DETECTOR

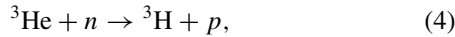
The SNO detector [9], shown schematically in Fig. 1, consisted of an inner volume containing 10^6 kg of 99.92% isotopically pure heavy water ($^2\text{H}_2\text{O}$, hereafter referred to as D_2O) within a 12 m diameter transparent acrylic vessel (AV). Over $7 \times 10^6 \text{ kg}$ of H_2O between the rock and the AV shielded the D_2O from external radioactive backgrounds. An array of 9456 inward-facing 20 cm Hamamatsu R1408 photomultiplier tubes (PMTs), installed on an 17.8 m diameter stainless steel geodesic structure (PSUP), detected Cherenkov radiation produced in both the D_2O and H_2O . A nonimaging light concentrator [10] mounted on each PMT increased the effective photocathode coverage to nearly 55% of 4π . The PMT thresholds were set to 1/4 of the charge from a single photoelectron. The inner $1.7 \times 10^6 \text{ kg}$ of H_2O between the AV and the PSUP shielded the D_2O against radioactive backgrounds from the PSUP and PMTs. Extensive purification systems removed radioactive isotopes from both the D_2O and the H_2O [11].

The detector was located in Vale's Creighton mine ($46^\circ 28' 30'' \text{ N}$ latitude, $81^\circ 12' 04'' \text{ W}$ longitude) near Sudbury, Ontario, Canada, with the center of the detector at a depth of 2092 m (5890 ± 94 meters water equivalent). At this depth, the rate of cosmic-ray muons entering the detector was approximately three per hour. Ninety-one outward-facing PMTs attached to the PSUP detected cosmic-ray muons. An offline veto based on information from these PMTs significantly reduced cosmogenic backgrounds.

The recoil electrons from both the ES and CC reactions were detected directly through their production of Cherenkov light. The total amount of light detected by the PMT array was correlated with the energy of the interacting neutrino.

The SNO detector operated in three distinct phases distinguished by how the neutrons from the NC interactions were detected. In Phase I, the detected neutrons captured on deuterons in the D_2O releasing a single 6.25 MeV γ ray, and it was the Cherenkov light of secondary Compton electrons or e^+e^- pairs that was detected. In Phase II, 2×10^3 kg of NaCl were added to the D_2O , and the neutrons captured predominantly on ^{35}Cl nuclei, which have a much larger neutron capture cross section than deuterium nuclei, resulting in a higher neutron detection efficiency. Capture on chlorine also released more energy (8.6 MeV) and yielded multiple γ rays, which aided in identifying neutron events. In Phase III, an array of proportional counters (the neutral current detection, or NCD, array) was deployed in the D_2O [12].

The proportional counters were constructed of approximately 2 m long high purity nickel tubes welded together to form longer “strings”. Neutrons were detected via the reaction



where the triton and proton had a total kinetic energy of 0.76 MeV, and traveled in opposite directions. The NCD array consisted of 36 strings filled with 3He , and an additional four strings filled with 4He that were insensitive to the neutron signals and were used to study backgrounds. Energetic charged particles within the proportional counters produced ionization electrons, and the induced voltage caused by these electrons was recorded as a function of time, referred to as a waveform. To increase the dynamic range, the waveform was logarithmically amplified before being digitized [12].

III. COMBINED ANALYSIS

In this article we present an analysis that combines data from all three phases of the SNO experiment. We include a new analysis of the data from Phase III of the experiment with pulse shape discrimination to distinguish neutrons from background alphas and we make improvements to the previous analysis of the first two phases of the experiment [7]. The combination accounts for any correlations in the systematic uncertainties between phases. Therefore, this is a more complete analysis than can be obtained by combining independently the previous results for the first two phases [7] and an independent analysis of the third phase [13]. The data were split into day and night sets in order to search for matter effects as the neutrinos propagated through the Earth.

The general form of the analysis was a fit to Monte Carlo–derived probability density functions (PDFs) for each of the possible signal and background types. As with previous analyses of SNO data, the following four variables were calculated for each event recorded with the PMT array: the effective electron kinetic energy, T_{eff} , reconstructed under the hypothesis that the light was caused by a single electron; the cube of the radial position, r , divided by 600 cm, $\rho = (r[\text{cm}]/600)^3$; the isotropy of the detected light, β_{14} ; and the angle of the reconstructed electron propagation relative to the direction of the Sun, $\cos \theta_\odot$. Different algorithms to calculate both T_{eff} and ρ were used for the first two phases and the third phase. References [7,13,14] contain detailed descriptions of

how these variables were calculated. The energy deposited in the gas of a proportional counter, E_{NCD} , was calculated for each event recorded with the NCD array, and the correlated waveform was determined [13].

Although there were multiple sets of data in this fit, the result was a single Φ_B and energy-dependent ν_e survival probability as described in Sec. III A. We summarize the event selection and backgrounds in Sec. III B. Sections III C and III D, respectively, describe the PDFs and efficiencies. The method for combining the multiple sets of data in a single analysis is presented in Sec. III E. Finally, Sec. III F outlines the alternative analyses to verify the combined analysis.

A. Parametrization of the 8B neutrino signal

We fitted the neutrino signal based on an average Φ_B for day and night, a ν_e survival probability as a function of neutrino energy, E_ν , during the day, $P_{ee}^d(E_\nu)$, and an asymmetry between the day and night survival probabilities, $A_{ee}(E_\nu)$, defined by

$$A_{ee}(E_\nu) = 2 \frac{P_{ee}^n(E_\nu) - P_{ee}^d(E_\nu)}{P_{ee}^n(E_\nu) + P_{ee}^d(E_\nu)}, \quad (5)$$

where $P_{ee}^n(E_\nu)$ was the ν_e survival probability during the night. This was the same parametrization as we used in our previous analysis of data from Phases I and II [7]. This analysis assumes a constant flux of 8B neutrinos produced by the Sun. We have published previous analyses that show no evidence for periodicity in the flux of 8B neutrinos produced by the Sun [15].

Monte Carlo simulations assuming the standard solar model and no neutrino oscillations were used to determine the event variables for 8B neutrino interactions in the detector. These simulations were then scaled by the factors given in Table I.

Unlike our earlier publications [8,14,16], this parametrization included a constraint on the rate of ES interactions relative to the rate of CC interactions based on their relative cross sections. It also had the advantage that the fitted parameters [Φ_B , $P_{ee}^d(E_\nu)$, and $A_{ee}(E_\nu)$] were all directly related to the scientific questions under investigation. Moreover, it disentangled the detector response from the fit result as $P_{ee}^d(E_\nu)$ and $A_{ee}(E_\nu)$ were functions of E_ν as opposed to T_{eff} .

Appendix A explains how this parametrization can be used to describe sterile neutrino models that do not predict any day/night asymmetry in the sterile neutrino flux and

TABLE I. 8B neutrino interactions scaling factors.

Interaction	Day/Night	Scaling factor
CC, ES_e	Day	$\Phi_B P_{ee}^d(E_\nu)$
$ES_{\mu\tau}$	Day	$\Phi_B [1 - P_{ee}^d(E_\nu)]$
CC, ES_e	Night	$\Phi_B P_{ee}^n(E_\nu)$
$ES_{\mu\tau}$	Night	$\Phi_B [1 - P_{ee}^n(E_\nu)]$
NC	Day + Night	Φ_B

do not predict any distortion in the sterile E_ν spectrum.¹ Reference [18] presents a very general sterile neutrino analysis that includes day versus night asymmetries.

Due to the broad T_{eff} resolution of the detector, $P_{ee}^d(E_\nu)$ was not sensitive to sharp distortions and was parametrized by

$$P_{ee}^d(E_\nu) = c_0 + c_1(E_\nu[\text{MeV}] - 10) + c_2(E_\nu[\text{MeV}] - 10)^2, \quad (6)$$

where c_0 , c_1 , and c_2 were parameters defining the ν_e survival probability. Simulations showed that the fit was not sensitive to higher order terms in the polynomial. Expanding the function around 10 MeV, which corresponds approximately to the peak in the detectable ^8B neutrino E_ν spectrum, reduced correlations between c_0 , c_1 , and c_2 . For the same reasons, $A_{ee}(E_\nu)$ was parametrized by

$$A_{ee}(E_\nu) = a_0 + a_1(E_\nu[\text{MeV}] - 10), \quad (7)$$

where a_0 , and a_1 were parameters defining the relative difference between the night and day ν_e survival probability. By disallowing sharp changes in the neutrino signal that can mimic the background events at low energies, these parametrizations reduced the covariances between the neutrino interaction and background rates.

To correctly handle ES events, we simulated ν_μ s with the same E_ν spectrum as ν_e s, such that scaling factors for these interactions in Table I were satisfied. In our previous analysis [7] we approximated the ν_μ and ν_τ cross section by 0.156 times the ν_e cross section, and then included an additional systematic uncertainty to account for the fact that the ratio of the ν_e to ν_μ ES cross section is not constant as a function of E_ν .

B. Event selection and backgrounds

Table II summarizes the data periods used in this analysis. We used the same periods of data as our most recent analyses of data from these phases [7,8].

Event cuts to select good candidates were identical to those in the previous analyses of these data [7,8]. The following cuts on the event variables were applied: $\rho < (550[\text{cm}]/600[\text{cm}])^3 = 0.77025$, $-0.12 < \beta_{14} < 0.95$, $3.5 \text{ MeV} < T_{\text{eff}} < 20.0 \text{ MeV}$ for Phases I and II, and $6.0 \text{ MeV} < T_{\text{eff}} < 20.0 \text{ MeV}$ for Phase III. After these cuts the data consisted of events from ES, CC, and NC interactions of ^8B neutrinos, and a number of different background sources.

Radioactive decays produced two main background types: “electron-like” events, which resulted from β particles or γ rays with a total energy above our T_{eff} threshold, and neutrons produced by the photodisintegration of deuterons by γ rays with energies above 2.2 MeV. During Phase III, only the neutron events were observed from radioactive background decays, due to the higher T_{eff} threshold for that phase.

TABLE II. Dates for the data in the different phases used in this analysis.

Phase	Start date	End date	Total time [days]	
			Day	Night
I	November 1999	May 2001	119.9	157.4
II	July 2001	August 2003	176.5	214.9
III	November 2004	November 2006	176.6	208.6

The radioactive decays of ^{214}Bi and ^{208}Tl within the regions of the detector filled with D_2O and H_2O were major sources of background events. ^{214}Bi is part of the ^{238}U decay chain, but it was most likely not in equilibrium with the early part of the decay chain. The most likely source of ^{214}Bi was from ^{222}Rn entering the D_2O and H_2O from mine air. ^{208}Tl is part of the ^{232}Th decay chain. These sources of radiation produced both electron-like events and photodisintegration neutrons. *Ex situ* measurements [19,20] of background levels in the D_2O and H_2O provided constraints on the rate of these decays, as given in Tables XIX and XX of Appendix C.

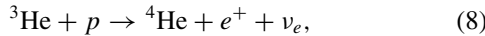
Background sources originating from the AV included decays of ^{208}Tl within the acrylic, which produced both electron-like events and photodisintegration neutrons. In addition, radon progeny that accumulated on the surface of the AV during construction could create neutrons through (α, n) reactions on isotopes of carbon and oxygen within the AV. Near the T_{eff} threshold in Phases I and II the majority of background events originated from radioactive decays within the PMTs.

Due to the dissolved NaCl in the D_2O during Phase II, calibration sources that produced neutrons, and other sources of neutrons, led to the creation of ^{24}Na via neutron capture on ^{23}Na . ^{24}Na decays with a half-life of approximately 15 h, producing a low energy β particle and two γ rays. One of these γ rays has an energy of 2.75 MeV, which could photodisintegrate a deuteron. This resulted in additional electron-like events and photodisintegration neutrons during Phase II. Periods after calibrations were removed from the data, but there were remaining backgrounds.

During Phase III there were additional photodisintegration neutron backgrounds due to radioactivity in the nickel and cables of the NCD array, as well as two “hotspots” on the strings referred to as K2 and K5. The estimated number of these background events, given in Table XX of Appendix C, were based on previous analyses of these data [13] except for backgrounds from the K5 hotspot, which was based on a recent reanalysis [21]. The previously estimated number of neutrons observed in the NCD array due to the K5 hotspot was 31.6 ± 3.7 , which assumed there was Th and a small amount of U in the hotspot based on both *ex situ* and *in situ* measurements. Based on measurements performed on the strings after they were removed from the D_2O , it was determined that the radioactivity was likely on the surface and most likely pure Th with very little U. This resulted in a new estimate of $45.5^{+7.5}_{-8.4}$ neutron background events observed in the NCD array from this hotspot.

¹In our previous analysis of data from Phases I and II [7] we described this method as imposing a unitarity constraint, which was not technically correct.

Aside from the radioactive decay backgrounds, there were additional backgrounds to the ^8B neutrino measurement due to ν_e s produced by the following reaction:



in the Sun, so-called *hep* neutrinos. These have a maximum energy of 18.8 MeV, which is slightly above the ^8B neutrino maximum energy of 15 MeV, and the standard solar model (SSM) prediction for their flux is approximately one thousand times smaller than Φ_B [22]. Estimates of this background were based on the SSM prediction including the effects of neutrino oscillations obtained from previous analyses [7]. There were instrumental backgrounds that reconstructed near the AV. Above $T_{\text{eff}} \approx 6$ MeV these events formed a distinct peak at low values of β_{14} , so they were easily removed by the cuts on β_{14} and ρ . At lower T_{eff} , position reconstruction uncertainties increase, and the β_{14} distribution of these “AV instrumental background” events broadens, resulting in incomplete removal by these cuts. This background was negligible in Phase III due to the higher T_{eff} threshold used for the analysis of data from that phase. Finally, there were also background events due to neutrinos produced by particle decays in the atmosphere. The estimated numbers for these background events, given in Tables XIX and XX of Appendix C, were based on previous analyses of these data [7,13].

C. PDFs

For Phases I and II the event variables T_{eff} , ρ , β_{14} , and $\cos \theta_\odot$ were used to construct four-dimensional PDFs. For Phase III the reduced number of NC events observed with the PMT array made the β_{14} event variable unnecessary, so the PDFs were three-dimensional in the remaining three event variables. Monte Carlo simulations were used to derive the PDFs for all signal and background classes observed with the PMT array except for backgrounds originating from radioactivity in the PMTs, which was described by an analytical function. Compared to the previous analysis of data from Phases I and II [7], we increased the number of Monte Carlo events for the CC and ES interactions by a factor of four, and for NC interactions and some background types by a factor of two.

The Monte Carlo simulation was verified using a variety of calibration sources. Based on these comparisons a number of systematic uncertainties were defined to represent possible variations in the event variables relative to the calibrations. In general these included differences in the offset, scale, and resolution for each of the event variables. Appendix C gives the complete list of systematic uncertainties associated with the PDFs. Except where specified these uncertainties were the same as those used in the most recent analyses of these data [7,13].

Extensive calibrations using a ^{16}N γ -ray source [23], which produced electrons with kinetic energies of approximately 5.05 MeV from Compton scattering, allowed us to calibrate T_{eff} . In Phase I the linearity of T_{eff} with respect to electron kinetic energy was tested using a proton-triton fusion γ -ray source [24], which produced electrons with kinetic energies up to approximately 19.0 MeV from Compton scattering and

pair-production. Based on these sources, we parametrized the reconstructed electron kinetic energy including a possible nonlinearity by

$$T'_{\text{eff}} = T_{\text{eff}} \left(1 + c_0^E \frac{T_{\text{eff}}[\text{MeV}] - 5.05}{19.0 - 5.05} \right), \quad (9)$$

where c_0^E represents the level of nonlinearity. The linearity in all phases was tested using the following two electron sources: a ^8Li calibration source [25] that produced electrons with a continuous distribution up to approximately 13 MeV; and electrons with a continuous energy distribution up to approximately 50 MeV produced by the decay of muons that stopped within the AV. These studies revealed non-linearities consistent with zero. We assumed any nonlinearities below our level of sensitivity were correlated between all three phases, and we used a value of $c_0^E = 0 \pm 0.0069$, which was equal to the value used in the previous analysis of data from Phases I and II [7].

During Phase III, radioactive $^{24}\text{NaCl}$ brine was injected into the D_2O on two separate occasions [26]. The brine was thoroughly mixed in the D_2O and provided a uniformly distributed source of γ rays, allowing us to study possible T_{eff} variations in regions that were previously not sampled due to the restricted movement of the ^{16}N source. The observed variation in the event rate of ^{24}Na decays within the fiducial volume of solar neutrino analysis was consistent with what was allowed by the T_{eff} calibration parameters determined with the ^{16}N source at $T_{\text{eff}} > 6$ MeV.

While the intrinsic rate of radioactive backgrounds from solid bulk materials such as the acrylic vessel or PMT array were not expected to vary over the course of the experiment, variations in detector response make the detected rates vary over time, and because of differences in the live-time fractions between day and night, these variations were aliased into day/night differences. PDFs derived from Monte Carlo naturally include day/night detector asymmetries because the detector simulation tracks changes to the detector response. Our previous analysis derived the analytical PDFs for radioactivity originating from the PMTs using a bifurcated analysis of real data with the day and night data combined [7], which did not account for possible day/night asymmetries.

To accommodate such asymmetries in the present analysis we allowed different observed background rates between day and night, and we repeated the bifurcated analysis with the data separated into day and night sets. Similarly to the previous analysis [7] the PDF was parameterized by the following function:

$$P_{\text{PMT}}(T_{\text{eff}}, \beta_{14}, \rho) = e^{\epsilon T_{\text{eff}}} (e^{\nu \rho} + |b + 1| - 1) \times \mathcal{N}(\beta_{14} | \omega_0 + \omega_1(\rho - 0.61), \beta_s), \quad (10)$$

where ϵ , ν , b , ω_0 , ω_1 , and β_s were parameters determined from the fit to the bifurcated data. $\mathcal{N}(x | \bar{x}, \sigma)$ represents a Gaussian distribution in x with mean \bar{x} and standard deviation σ . The uncertainties in the radial parameters were obtained from one dimensional scans of the likelihood function because the magnitude operator distorted the likelihood function at $b = -1$. Compared to the function used in the previous analysis [7], $\omega_1 \rho$ was replaced with $\omega_1(\rho - 0.61)$ to reduce the correlation between ω_0 and ω_1 . Table III lists the PDF parameters from

TABLE III. PMT background PDF parameters as determined by a bifurcated analysis. ρ_{vb} is the correlation between the ν and b parameters.

Parameter	Phase			
	I-day	I-night	II-day	II-night
ϵ	-6.7 ± 1.3	-5.6 ± 1.0	-6.3 ± 0.9	-7.0 ± 0.9
ν	6.6 ± 0.9	6.8 ± 1.5	5.3 ± 1.0	5.7 ± 1.1
b	-1.0 ± 1.3	3.3 ± 12.0	-0.3 ± 2.1	0.5 ± 3.0
ρ_{vb}	0.60	0.96	0.91	0.94

this analysis. We observed a weak day/night asymmetry in these results, in particular at roughly the 1σ level in the T_{eff} spectrum. Figure 2 shows the fits to the T_{eff} spectrum for Phase I.

The E_ν spectrum of ^8B neutrinos used to derive the PDFs for ES, CC, and NC interactions was obtained, including the uncertainties, from Ref. [27]. Our previous analysis of data from Phases I and II [7] included this uncertainty for the CC and ES PDFs. In this analysis we also included the effects of this uncertainty on the normalization of the NC rate.

D. Efficiencies

Table XXII in Appendix C lists the uncertainties associated with neutron detection. The majority of these were identical to previous analyses of these data [7,13] except where indicated below.

We recently published [13] an analysis based on calibration data from Phase III that determined that the fraction of neutrons created in NC interactions that were detectable with the PMT array, ϵ_n^{PMT} , was 0.0502 ± 0.0014 . The previous analysis of data from Phase III [8] used $\epsilon_n^{\text{PMT}} = 0.0485 \pm 0.0006$, which relied on a Monte Carlo based method to determine the uncertainty on the neutron detection efficiency. This new analysis avoids the dependence on Monte Carlo simulations.

Similarly, a calibration based method was used to calculate the fraction of neutrons created by NC interactions that

were captured in the gas of the NCD array, ϵ_n^{NCD} . This yielded $\epsilon_n^{\text{NCD}} = 0.211 \pm 0.005$ [13], which had slightly better precision than the value of $\epsilon_n^{\text{NCD}} = 0.211 \pm 0.007$ used in the previous analysis of data from Phase III [8]. We multiplied ϵ_n^{NCD} by a correction factor of 0.862 ± 0.004 in order to determine the efficiency for detecting NC interactions in the NCD array. The correction factor, averaged over the duration of Phase III, included the mean live fraction of the signal processing systems, threshold efficiencies, and signal acceptance due to event selection cuts.

This analysis corrected a 1.2% error in the normalization of the number of NC events observed in the PMT array that was in the previous analysis of data from Phase III [8]. Because the majority of NC events were observed in the NCD array, this normalization error had a relatively small effect on the measured NC flux. In addition we have corrected a 0.1% error in the deuteron density used for that analysis.

E. Description of the fit

The combined fit to all phases was performed using the maximum likelihood technique, where the negative log likelihood function was minimized using MINUIT [28]. The events observed in the PMT and NCD arrays were uncorrelated, therefore the negative log likelihood function for all data was given by

$$-\log L_{\text{data}} = -\log L_{\text{PMT}} - \log L_{\text{NCD}}, \quad (11)$$

where L_{PMT} and L_{NCD} , respectively, were the likelihood functions for the events observed in the PMT and NCD arrays.

The negative log likelihood function in the PMT array was given by

$$-\log L_{\text{PMT}} = \sum_{j=1}^N \lambda_j(\vec{\eta}) - \sum_{i=1}^{n_{\text{PMT}}} \log \left[\sum_{j=1}^N \lambda_j(\vec{\eta}) f(\vec{x}_i | j, \vec{\eta}) \right], \quad (12)$$

where N was the number of different event classes, $\vec{\eta}$ was a vector of “nuisance” parameters associated with the systematic uncertainties, $\lambda_j(\vec{\eta})$ was the mean of a Poisson distribution for the j th class, \vec{x}_i was the vector of event variables for event i , n_{PMT} was the total number of events in the PMT array during the three phases, and $f(\vec{x}_i | j, \vec{\eta})$ was the PDF for events of type j .

The PDFs for the signal events were re-weighted based on Eqs. (6) and (7). This was a CPU intensive task that was prohibitive for the kernel based PDFs used in the previous analysis of data from Phases I and II [7]. Therefore, in that analysis, the PDFs were also binned based on E_ν , and these PDFs were then weighted by the integral of Eqs. (6) and (7) within that bin. This analysis did not require this approximation when calculating the best fit, although an approximation was used when “scanning” (described below) the systematic uncertainties. As described in Ref. [18], $\lambda(\vec{\eta})$ was reparametrized such that the Monte Carlo-based PDFs did not need to be normalized.

In the previous analysis of the PMT array data from Phase III [8], the nuisance parameters were only propagated on

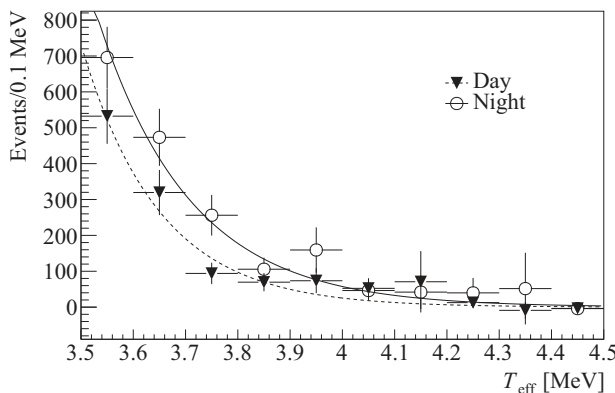


FIG. 2. T_{eff} spectra for the PMT background events obtained from a bifurcated analysis of data from Phase I including the best fits to Eq. (10).

the PDFs for neutrino interactions, while this analysis also propagates these parameters on the PDFs for background events. Because the number of background events observed in the PMT array was small relative to the number of neutrino events, this had a relatively minor effect on that result.

The negative log likelihood function in the NCD array was given by

$$-\log L_{\text{NCD}} = \frac{1}{2} \left(\frac{\sum_{j=1}^N \nu_j(\vec{\eta}) - n_{\text{NCD}}}{\sigma_{\text{NCD}}} \right)^2, \quad (13)$$

where $\nu_j(\vec{\eta})$ was the mean of a Poisson distribution for the j^{th} class, n_{NCD} was the total number of neutrons observed in the NCD array based on the fit described in Sec. IV B, and σ_{NCD} was the associated uncertainty.

The mean number of events for a given class was often related to the mean number of events for another class; for instance, the number of ES, CC, and NC events in each phase were determined from the parameters in Sec. III A.

Constraints were placed on various nuisance parameters and the rate of certain classes of background events. Including these constraints, the negative log likelihood function was given by

$$-\log L = -\log L_{\text{data}} + \frac{1}{2}(\vec{\eta} - \vec{\mu})^T \Sigma^{-1}(\vec{\eta} - \vec{\mu}), \quad (14)$$

where $\vec{\eta}$ was the value of the nuisance parameters, $\vec{\mu}$ was the constraint on the parameters, and Σ was the covariance matrix for the constraints. Appendix C lists all of the constraints.

Our previous analysis of data from Phases I and II [7] imposed a physical bound on background rates, so that they were not allowed to become negative in the fit. Without these bounds the background from neutrons originating from the AV in Phase II favors a rate whose central value was negative, but consistent with zero. The uncertainty in the PDFs due to the finite Monte Carlo statistics could explain the fitted negative value. The previously reported ensemble tests [7] used a central value for this background that was more than two statistical standard deviations above zero, such that no significant effect from the bound was observed. Using a positive bound for the backgrounds when ensemble testing with Monte Carlo data that does not contain any neutrons originating from the AV in Phase II tends to shift Φ_B down on average compared to the flux used to simulate the data, as we only obtained background rates that were equal to or higher than the values used in the simulations. Removing this bound allowed closer agreement between the expectation values for the signal parameters and the values used in the simulated data. We removed the bound that forced the background to be positive, facilitating the combination of the SNO results with other experiments.

In the previous analysis of data from Phases I and II [7] the background constraints obtained for the average of the day and night rate (e.g., for the *ex situ* measurements of ^{214}Bi and ^{208}Tl) were applied independently to both the day and the night rates, which resulted in a narrower constraint on these backgrounds than we intended. This analysis correctly applies this as a day and night averaged constraint.

Three methods for handling the nuisance parameters were used. Some were “floated,” i.e., allowed to vary within the MINUIT minimization of the negative log likelihood function. Others were “scanned,” where a series of fits were performed with different values of the parameter in order to find the best fit. This process was repeated for all scanned nuisance parameters multiple times to converge on the global minimum of the fit. The scanning method gives the same results as the floating method, but was computationally faster for parameters that were not highly correlated. Finally, some were shifted by plus and minus one sigma about the central value (shift-and-refit) and the effect of the nuisance parameter was included in the calculation of the uncertainty. The method used for each nuisance parameter was determined based on ensemble tests, which established the magnitude of the effect on Φ_B and the ν_e survival probability parameters. The nuisance parameters with significant effects were floated or scanned. Appendix C lists how each nuisance parameter was treated.

In addition to the systematic uncertainties considered in previous analyses, this analysis also included a systematic uncertainty due to the finite Monte Carlo statistics used to construct the PDFs. We performed 1000 independent fits in which the number of events in each bin of the PDF were drawn from a Poisson distribution. The uncertainty due to the finite Monte Carlo statistics was determined from the distribution of the fit parameters.

In order to calculate the total systematic uncertainty on the Φ_B and the ν_e survival probability parameters, we applied the shift-and-refit 100 times for each parameter in order to calculate the asymmetrical likelihood distribution for that parameter. We then performed one million fits with the nuisance parameters drawn randomly from these distributions. The total systematic uncertainty was obtained from the resulting distribution of the fit results. This is the first time we have applied this procedure, which correctly accounts for the combination of asymmetrical uncertainties. In order to calculate the effects of the day/night or MC systematic uncertainties, respectively, this procedure was repeated with only the nuisance parameter related to day/night differences or MC statistics varied.

In total the fit included Φ_B , the five ν_e survival probability parameters described in Sec. III A, 36 background rate parameters, 35 floated or scanned nuisance parameters, and 82 shift-and-refit nuisance parameters.

The biases and uncertainties obtained from this analysis method were tested using simulated data. The number of simulated sets of data was restricted by the amount of Monte Carlo data available. For simulated data containing neutrino interactions and some background classes, we did bias tests with 250 sets of data. For simulated data containing neutrino interactions and all background classes, we did bias tests with 14 sets of data. All of these tests showed the method was unbiased and produced uncertainties consistent with frequentist statistics.

F. Crosschecks

As a crosscheck on the analysis method described above, we developed two independent analyses. The first crosscheck

compared the results from the above method run only on data from Phases I and II. This was crosschecked against the method described in the previous analysis of this data [7] with the improvements described in Sec. III E above also included in the analysis using the previous method. The results from the two methods were in agreement.

We developed an alternate Bayesian based analysis where the posterior probability distribution was sampled using a Markov Chain Monte Carlo (MCMC). This analysis was applied to data from Phase III, using the results from the maximum likelihood analysis performed on data from Phases I and II as a prior. The priors for background and neutrino interaction rates had zero probability for negative rates and were uniform for positive rates. There were two important differences between this alternate analysis and the maximum likelihood method described above. Firstly, because the systematic uncertainties were varied in each step of the MCMC, the uncertainties included all systematic and statistical uncertainties. Secondly, this method samples the entire posterior probability distribution instead of identifying the maximum likelihood. Reference [29] provides details of this method. As shown in Sec. V the results of the Bayesian and maximum likelihood fits agreed. An alternate Bayesian analysis was also performed with details provided in Reference [30]. This analysis was completed after the other analyses presented in this paper and therefore was not used as a detailed crosscheck; however, the results were consistent with the results presented here.

IV. NCD ARRAY ANALYSIS

The NCD array observed neutrons, alphas, and events caused by instrumental backgrounds. Because of their low stopping power in the gas of the proportional counters, electrons rarely triggered the NCD array. A series of cuts described in Ref. [13] removed the instrumental backgrounds. For neutron events E_{NCD} was peaked at approximately 0.76 MeV, with a maximum energy of 0.85 MeV when including the resolution. E_{NCD} was less than 0.76 MeV if the proton or triton hit the nickel walls before losing all their energy. We identified the following two major categories of α events: so-called bulk alphas, which came from radioactive decays occurring throughout the nickel bodies of the proportional counters due to the presence of U and Th and their progeny, and so-called surface alphas, coming from the decay of ^{210}Po , which was supported by ^{210}Pb that had plated onto the inner surface of the nickel bodies. Below 1.4 MeV both types of α events produced relatively flat E_{NCD} spectra. Due to differences in construction of the strings, the number of alpha events varied from string to string.

The previous analysis of data from Phase III [8] distinguished between neutron and α events by fitting the E_{NCD} spectrum. The PDF of E_{NCD} for neutron events was obtained from calibration data, and for alpha events it was obtained from simulations. Between 0.4 MeV and 1.4 MeV the fitted number of α and neutron events, respectively, were approximately 5560 and 1170. The large number of alpha events resulted in both a large statistical uncertainty, and a large systematic

uncertainty due to difficulties in accurately determining the PDF of E_{NCD} for α events.

The waveforms of neutron events could be significantly broader than those from alpha events, depending on the orientation of the proton-triton trajectory. This distinction was lessened by the significant tail in the waveforms caused by the long ion drift times. In an attempt to reduce the number of α events, and therefore the uncertainties associated with them, we developed four different particle identification (PID) parameters and a cut on these parameters. As described Sec. IV A, this cut reduced the number of events in the strings filled with ^4He (α events) by more than 98%, while maintaining 74.78% of the neutron events. Section IV B describes the fit to the E_{NCD} spectrum after this cut.

These analyses rely heavily on two calibration periods with a ^{24}Na source distributed uniformly throughout the detector [26], which produced neutrons similar to those from ^8B neutrino NC reactions. These calibrations were performed in 2005 and 2006, and were respectively referred to as ^{24}Na -2005 and ^{24}Na -2006. A composite source of ^{241}Am and ^9Be , referred to as AmBe, produced a point-like source of neutrons. This source was positioned throughout the detector during six significant calibration campaigns spanning Phase III. These data were useful for assessing systematic uncertainties associated with temporal and spatial variations in the neutron detection efficiency and PDF of E_{NCD} .

A. Particle identification in the NCD array

Before analyzing the waveforms, the effect of the logarithmic amplifier was removed using parameters determined from various calibration pulses in a process referred to as delogging [13].

Two particle identification parameters, p_a and p_b , were based on fitting the waveforms to libraries of known neutron and alpha waveforms. Each waveform was fitted to each library waveform based on a χ^2 method. The relative start time of the event and library waveforms was varied to find the minimum χ^2 . In both cases the fits did not extend to later times to avoid the effects of ion mobility. Both of these particle identification parameters were defined by

$$\log \left(\frac{\chi_\alpha^2}{\chi_n^2} \right), \quad (15)$$

where χ_α^2 and χ_n^2 , respectively, were the best χ^2 s from the α and neutron hypotheses. The libraries used to calculate p_a were primarily based on simulation [31], and the χ^2 was calculated between where the waveform first crossed a value equal to 10% of the peak value and where it first returned to 30% of the peak value [32]. Figure 3 shows some sample fits. This clearly shows the broad waveform for neutrons with a proton-triton trajectory that was roughly perpendicular to the anode, which allows them to be separated from alphas.

To calculate p_b , the neutron library was obtained from ^{24}Na -2005 data, and the α library was obtained from events on the strings filled with ^4He [33]. The χ^2 was calculated between where the waveform first crossed a value equal to 10% of the peak value and where it first returned to 40% of the peak value.

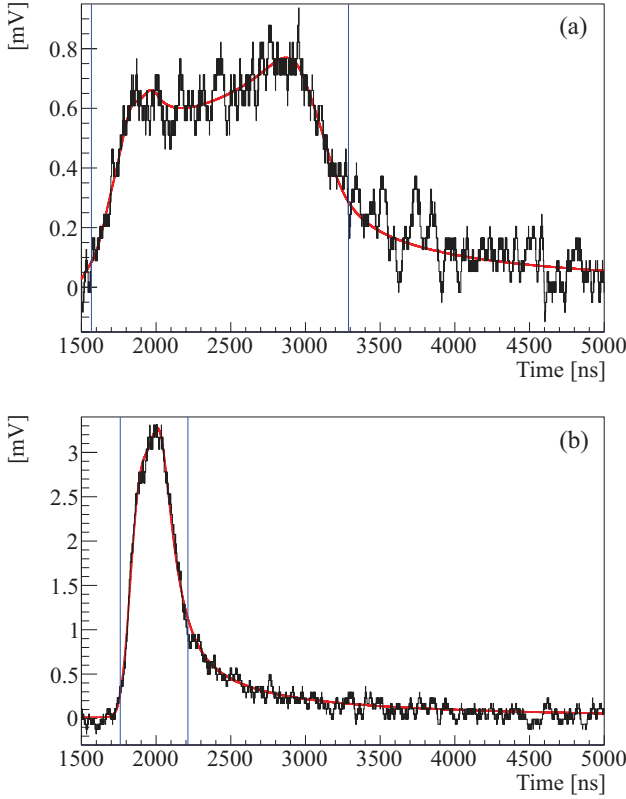


FIG. 3. (Color online) Sample waveforms. (a) shows a neutron waveform (black line) obtained from ^{24}Na calibration data with the best fit to the neutron hypothesis (thick-red line). (b) shows an α waveform (black line) obtained from a string filled with ^4He with the best fit to the α hypothesis (thick-red line). The vertical lines represent the fit boundaries.

The libraries for this parameter included events that were used in later studies to evaluate performance. We excluded fitting a waveform to itself because this would result in a χ^2 equal to zero, i.e., a perfect match.

The remaining two particle identification parameters, p_c and p_d , were respectively based on the kurtosis and skewness of the waveform after smoothing the waveform and deconvolving the effects of ion mobility assuming an ion drift time of 16 ns. The skewness and kurtosis were calculated using the region between where the waveform first crossed a value equal to 20% of the maximum and where it first returned to 20% of the peak value.

Figure 4 shows the distribution of the particle identification parameters for known neutron and alpha events. The left plot shows that p_a and p_b were highly correlated, which was unsurprising given their similar definitions. This plot also shows that a cut on these two parameters (PID cut 1) removes almost all alpha events while preserving the majority of neutron events. This cut selected events where the alpha hypothesis was significantly worse than the neutron hypothesis. After this cut, we recovered approximately 5% of the neutron events with a second cut on p_c and p_d (PID cut 2). PID cut 2 was only applied to events that failed PID cut 1, and selected events with high skewness (p_d) or low kurtosis

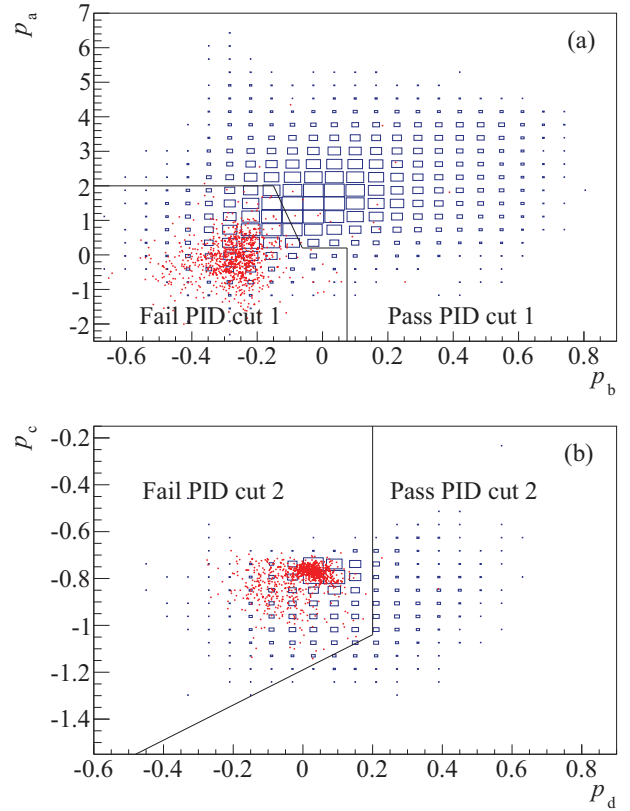


FIG. 4. (Color online) Distribution of particle identification parameters for neutron events (boxes, where the area represents the number of events) and α events (red marks). The line represents the boundary for cuts. PID cut 1 applies to parameters p_a and p_b (a), and PID cut 2 applies to parameters p_c and p_d for events that failed PID cut 1 (b).

(p_c), i.e. the waveforms were not symmetric in time or had a relatively flat peak. This combined cut, selecting events that passed PID cuts 1 or 2, was used for the rest of this analysis.

Figure 5 shows that the particle identification cut removes almost all the events on the strings filled with ^4He , i.e., α events, while maintaining the majority of the ^{24}Na calibration events, i.e., neutron events. This also shows that the fraction of α events removed by the particle identification cut was relatively constant as a function of E_{NCD} . The right most plot of Fig. 5 shows that the α background was significantly reduced, leaving what was clearly mostly neutron events.

Figure 6 shows the fraction of neutron events surviving the combined particle identification cut, ϵ_{PID} , as a function of neutron capture string for ^{24}Na -2005 and ^{24}Na -2006 data. Table IV shows the average obtained from these measurements. The high χ^2/NDF obtained with the ^{24}Na -2006 data suggests a slight variation in ϵ_{PID} as a function of string; however, the correlation between the ϵ_{PID} calculated for each string between the 2005 and 2006 calibrations was only 0.159, which was so small that it suggested random string-to-string variation instead of a feature of the NCD array.

Table V summarizes the systematic uncertainties associated with ϵ_{PID} . Based on the methods for deriving these systematic uncertainties, we assumed most correlations were zero. A

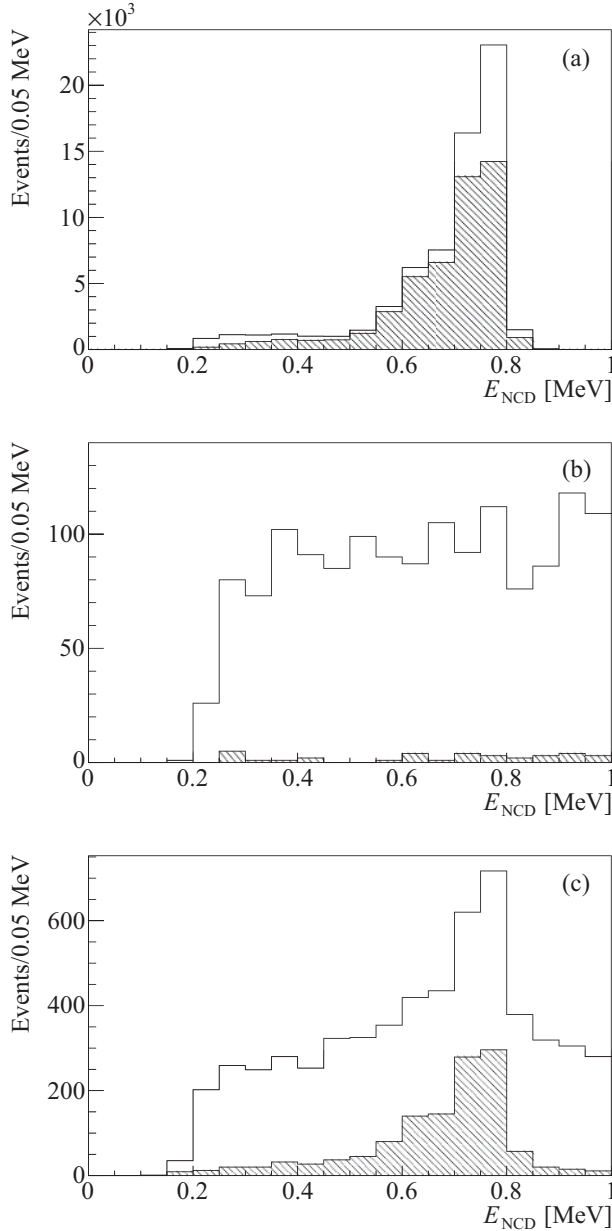


FIG. 5. E_{NCD} spectrum before (white) and after (hashed) the particle identification cut. (a) is for ^{24}Na calibration data (neutrons). (b) is for data from strings filled with ^4He (alphas). (c) is for data from strings filled with ^3He .

correlation of 0.50 was assumed between the following pairs of systematic uncertainties: delogging and ^{24}Na uniformity, delogging and temporal variation, p_a correction and ^{24}Na uniformity, p_a correction and temporal variation, and p_a correction and delogging. Including these correlations the total absolute systematic uncertainty was 0.0065. Combining the systematic and statistical uncertainties in quadrature led to a total absolute uncertainty of 0.0068.

The ^{24}Na calibration data used to calculate ϵ_{PID} had a measured variation in the neutron production rate as a function of z position of less than 10% between the maximum and the value at $z = 0$. Figure 7 shows that the dependence of ϵ_{PID} with

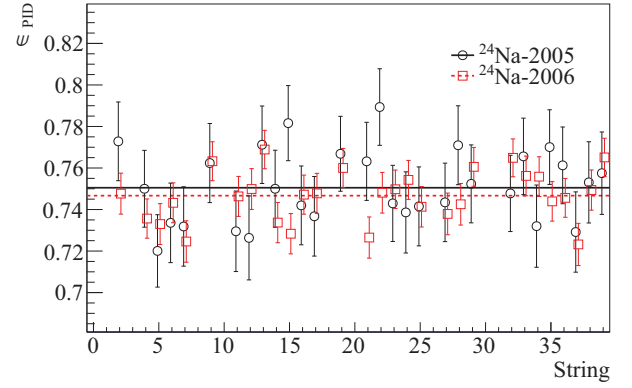


FIG. 6. (Color online) ϵ_{PID} as a function of string for the ^{24}Na calibration data. Fits to straight lines give 0.7505 ± 0.0035 with χ^2/NDF of 24.1/29 and 0.7467 ± 0.0018 with χ^2/NDF of 49.3/29, respectively.

source position, as measured with the AmBe data, was well approximated by a linear function with a maximum deviation compared to that at $z = 0$ of less than 0.01. Combining the possible nonuniformity in the ^{24}Na source distribution with the variation in ϵ_{PID} as a function of z position resulted in an absolute systematic uncertainty in ϵ_{PID} due to ^{24}Na uniformity of 0.0010. The variation due to the x and y position nonuniformity was accounted for in the string averaging used to calculate ϵ_{PID} .

The systematic uncertainty in ϵ_{PID} due to temporal variations was estimated based on the standard deviation of ϵ_{PID} calculated from the AmBe data averaged over all strings, and calculated at $z = 0$ assuming a linear dependence on z . The systematic uncertainty in ϵ_{PID} due to alpha events contaminating the ^{24}Na calibrations was estimated using the number of events with E_{NCD} between 0.9 MeV and 1.4 MeV as an estimate of the α contamination. The systematic uncertainty in ϵ_{PID} due to the delogging process was estimated by recalculating ϵ_{PID} with the individual delogging parameters shifted by their estimated uncertainties; because of possible correlations, the magnitude of the maximum shifts with each parameter were added together.

A correction to the p_a parameter based on ^{24}Na and AmBe data reduced the spatial and temporal variations in this parameter. A systematic uncertainty to account for the effect of this correction was estimated by calculating ϵ_{PID} assuming a one standard deviation shift in the correction to the p_a parameter and then combining the shifts caused by

TABLE IV. ϵ_{PID} obtained with the ^{24}Na -2005 and ^{24}Na -2006 data. The weighted average included a scaling of the uncertainty by $\sqrt{\chi^2/\text{NDF}}$ for the ^{24}Na -2006 data.

Data	ϵ_{PID}	χ^2/NDF
^{24}Na -2005	0.7505 ± 0.0035	24.1/29
^{24}Na -2006	0.7467 ± 0.0018	49.3/29
Weighted average	0.7478 ± 0.0019	

TABLE V. Absolute systematic uncertainties for ϵ_{PID} .

Systematic uncertainty	
^{24}Na uniformity	0.0010
Temporal variation	0.0037
Contamination	0.0019
De-logging	0.0018
p_a correction	0.0010
p_b neutron library	0.0019
Total	0.0065

each string in quadrature, which assumed that the corrections from string to string were not correlated.

The ^{24}Na -2005 data were used in both the neutron library used to calculate p_b , and in the determination of ϵ_{PID} . Although we did not expect this to bias the calculation of ϵ_{PID} , we conservatively included an additional absolute uncertainty of 0.0019, half the difference between ϵ_{PID} calculated with the ^{24}Na -2005 and ^{24}Na -2006 data.

B. Method for fitting the NCD array data

After the particle identification cut, the number of neutron events was determined from a likelihood fit to a histogram of E_{NCD} with 50 bins uniformly spaced between 0.4 and 0.9 MeV.

The PDF of E_{NCD} for neutron events was obtained from ^{24}Na -2006 data, and for α events it was approximated by

$$P_{\alpha}(E_{\text{NCD}}) = p_0 \left[P_0(E_{\text{NCD}}) + \sum_{n=1}^{N_{\text{max}}} p_n P_n(E_{\text{NCD}}) \right], \quad (16)$$

where p_0 and the p_n s were fit parameters, $P_n(E_{\text{NCD}})$ is the Legendre polynomial of order n : $P_0 = 1$, $P_1 = x$, $P_2 = 1/2(3x^2 - 1)$, $P_3 = 1/2(5x^3 - 3x)$, $P_4 = 1/8(35x^4 - 30x^2 + 3)$, with $x = 4(E_{\text{NCD}}[\text{MeV}] - 0.65)$. In order to ensure a well-defined PDF, negative values of this function were set to zero. The fit was repeated with different values for the systematic uncertainties associated with the E_{NCD} scale, a_1^{NCDE} , and resolution, b_0^{NCDE} , [see Eq. (C18) in Appendix C] selected from

a two-dimensional scan of these parameters. The point in this two-dimensional scan with the minimum χ^2 was chosen as the best fit point, and the systematic uncertainty associated with a_1^{NCDE} and b_0^{NCDE} was obtained from the maximum difference in the number of neutron events from the best fit point at the 1σ contour.

This fit was performed for values of N_{max} up to four, at which point, based on simulations, the polynomial started to fit to fluctuations in the data. We started with the assumption that a zeroth order polynomial was a satisfactory fit to the alpha background. If a higher order polynomial had a significant improvement in χ^2 then this became the new default, and this was tested against higher order polynomials. A significant improvement in χ^2 was defined as a decrease in χ^2 that would result in a 32% probability for accepting the higher order polynomial when the higher order was not a better model. This calculation included the fact that testing against many different higher order polynomials increases the chances of erroneously choosing a higher order polynomial, so a larger improvement in χ^2 was required. Reference [34] gives the changes in χ^2 defined as significant. This method was generic to any type of background, including instrumental backgrounds, provided they did not have features sharper than the assumed background shape.

We tested the bias of this method using simulated data. The mean number of neutron events in these sets of simulated data was based on the number of neutrons obtained from the previous analysis of data from Phase III [8] and ϵ_{PID} . The E_{NCD} values for these simulated neutron events were obtained from events that passed the particle identification cut in the ^{24}Na -2006 data.² The mean number of alpha events in these sets of simulated data was based on the number of alphas obtained from the previous analysis of data from Phase III [8] and the approximate fraction of α events removed by the particle identification cut. The E_{NCD} values for the simulated α events were obtained from events that passed the particle identification cut in the strings filled with ^4He . Because these strings did not have enough events, instead of using these events directly, we fitted the limited data to polynomials of the form in Eq. (16) with N_{max} varied from 1 to 4, and then used these polynomials to simulate as many E_{NCD} values as necessary. In order to test extreme possibilities for the alpha event E_{NCD} distributions, the highest order term from the fit was changed by plus and minus 2σ , resulting in the eight different PDFs shown in Fig. 8. The bias was less than 2% for all eight α PDFs.

Since only the ^{24}Na -2006 data were used to determine the PDF of E_{NCD} for neutrons, we included additional systematic uncertainties to account for changes in this PDF due to non-uniformity of the ^{24}Na source and possible temporal variations. The size of these systematic uncertainties were estimated using AmBe calibration data collected at various positions and times to calculate the PDF of E_{NCD} for neutron events, and then calculating the size of the shift in the reconstructed number of

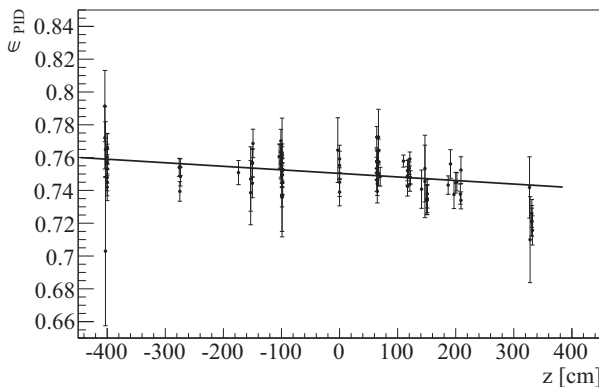


FIG. 7. ϵ_{PID} as function of z for a single string. This was typical of all strings.

²Note that for these tests the PDF of E_{NCD} for neutron events was created from the ^{24}Na -2005 data, unlike the fit to real data, which used the ^{24}Na -2006 data.

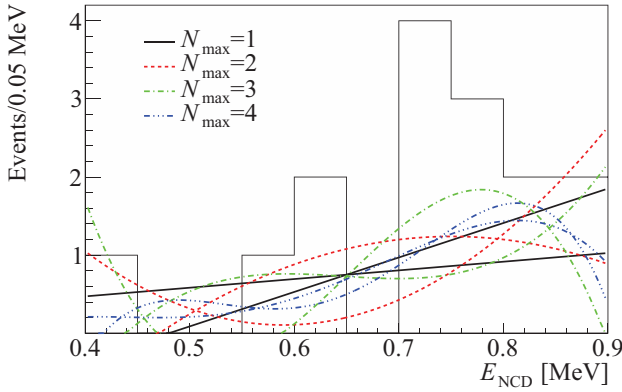


FIG. 8. (Color online) E_{NCD} spectrum for events on the strings filled with ^4He after the particle identification cut. The lines show the PDFs used to simulate α events for different values of N_{max} .

neutron events. The systematic uncertainties from the temporal and position variation were summed in quadrature to give a total systematic uncertainty of 0.64% on the number of neutrons obtained from the fit due to the PDF of E_{NCD} for neutron events.

V. RESULTS

Section V A presents the results from the analysis of data from the NCD array in Phase III. Because this was a new analysis of this data, we used a statistically limited and randomly selected one-third subset of the data to develop the particle identification cut and analysis. Once we had finalized all aspects of this analysis we fitted the entire set of data from the NCD array in Phase III. After completing this full analysis we realized that there was an error in the method to calculate the systematic uncertainty due to a_1^{NCDE} and b_0^{NCDE} , which was corrected in the results presented here.

The total number of neutron events detected in the NCD array obtained from this new analysis of data from Phase III was then used as a constraint in the fits to the combined data presented in Sec. V B. The combined analysis of the three phases also used a statistically limited and randomly selected one-third subset of the data to develop the fitting method. Once we had finalized all aspects of this analysis we fitted the entire set of data from all three phases.

A. Results from fit to NCD array data

Table VI shows the χ^2 and statistical uncertainty from the fit to the E_{NCD} spectrum for various values of N_{max} in Eq. (16). In general including extra terms in the PDF of E_{NCD} for α events should not result in best fits with higher χ^2 , but this can occur if the minimization routine finds different local minima. Based on our method for choosing the value of N_{max} representing the point where improvements in fit quality cease, the best fit occurs when $N_{\text{max}} = 4$. This corresponded to the maximum value of N_{max} considered before performing the fit, so to check that larger values of N_{max} did not produce better fits, we also fitted with N_{max} equal to five and six, as shown in Table VI. These fits did not produce better results.

TABLE VI. χ^2 and 1σ statistical uncertainty for various values of N_{max} in Eq. (16).

N_{max}	χ^2/NDF	Stat. uncertainty
0	54.92/48	4.2%
1	56.72/47	4.2%
2	47.63/46	5.5%
3	41.78/45	6.5%
4	40.20/44	6.9%
5	40.34/43	9.4%
6	40.41/42	9.2%

Figure 9 shows the best fit of the E_{NCD} spectrum. Although the best fit turns down at higher values of E_{NCD} the parameters were consistent with a flat PDF in that region. This variation in the allowed PDF was reflected in the increased statistical uncertainty with large N_{max} .

For the fit with $N_{\text{max}} = 4$ the systematic uncertainty due to a_1^{NCDE} and b_0^{NCDE} was five neutrons. Combining this with the systematic uncertainty in the PDF of E_{NCD} for neutrons, the statistical uncertainty in the fit, and dividing by ϵ_{PID} , the total number of neutrons observed in the NCD array equals 1115 ± 79 . The previous analysis of data from Phase III gave 1168 neutrons in the NCD array, with similar uncertainty [8]. That analysis had a large background due to alpha events, which made the assessment of the systematic uncertainty on the fitted number of events more challenging. The result presented here avoids that problem by eliminating most of the background from alpha events and allowing a very general PDF to describe the E_{NCD} spectrum for any remaining background events. Since the particle identification cut removed almost all alpha events, the fitted number of neutron events had a small to moderate correlation with the previous analysis of this data.

B. Results from combined fit to all data

For the combined fit to all data using the maximum likelihood technique, Table VII shows Φ_B and the ν_e survival

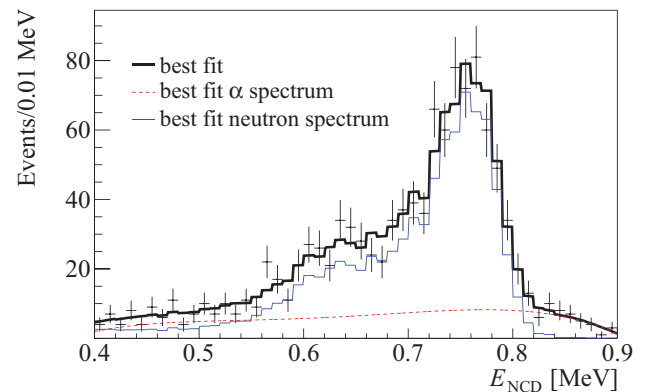


FIG. 9. (Color online) The fitted E_{NCD} spectrum after the particle identification cut.

TABLE VII. Results from the maximum likelihood fit. Note that Φ_B is in units of $\times 10^6 \text{ cm}^{-2} \text{ s}^{-1}$. The D/N systematic uncertainties includes the effect of all nuisance parameters that were applied differently between day and night. The MC systematic uncertainties includes the effect of varying the number of events in the Monte Carlo based on Poisson statistics. The basic systematic uncertainties include the effects of all other nuisance parameters.

	Best fit	Stat.	Systematic uncertainty			
			Basic	D/N	MC	Total
Φ_B	5.25	± 0.16	$+0.11$ -0.12	± 0.01	$+0.01$ -0.03	$+0.11$ -0.13
c_0	0.317	± 0.016	$+0.008$ -0.010	± 0.002	$+0.002$ -0.001	± 0.009
c_1	0.0039	$+0.0065$ -0.0067	$+0.0047$ -0.0038	$+0.0012$ -0.0018	$+0.0004$ -0.0008	± 0.0045
c_2	-0.0010	± 0.0029	$+0.0013$ -0.0016	$+0.0002$ -0.0003	$+0.0004$ -0.0002	$+0.0014$ -0.0016
a_0	0.046	± 0.031	$+0.007$ -0.005	± 0.012	$+0.002$ -0.003	$+0.014$ -0.013
a_1	-0.016	± 0.025	$+0.003$ -0.006	± 0.009	± 0.002	$+0.010$ -0.011

probability parameters as defined in Eqs. (6) and (7) of Sec. III A. Table VIII shows the correlation between these parameters. The combined fit to all data from SNO yielded a total flux of active neutrino flavors from ^8B decays in the Sun of $\Phi_B = (5.25 \pm 0.16(\text{stat.})^{+0.11}_{-0.13}(\text{syst.})) \times 10^6 \text{ cm}^{-2} \text{ s}^{-1}$. During the day the ν_e survival probability at 10 MeV was $c_0 = 0.317 \pm 0.016(\text{stat.}) \pm 0.009(\text{syst.})$, which was inconsistent at very high significance with the null hypothesis that there were no neutrino oscillations. Using the covariance matrix obtained from this combined analysis we can compare the best fit to various null hypotheses. The null hypothesis that there were no spectral distortions of the ν_e survival probability (i.e., $c_1 = 0$, $c_2 = 0$, $a_0 = 0$, $a_1 = 0$), yielded $\Delta\chi^2 = 1.97$ (26% C.L.) compared to the best fit. The null hypothesis that there were no day/night distortions of the ν_e survival probability (i.e., $a_0 = 0$, $a_1 = 0$), yielded $\Delta\chi^2 = 1.87$ (61% C.L.) compared to the best fit.

Figure 10 shows the RMS spread in $P_{ee}^d(E_\nu)$ and $A_{ee}(E_\nu)$, taking into account the parameter uncertainties and correlations. This figure also shows that the maximum likelihood analysis was consistent with the alternative Bayesian analysis. Table XIII contains the results from the Bayesian analysis.

Figures 11–13, respectively, show one-dimensional projections of the fit for Phases I, II, and III. In each figure the fitted background (Bkg) is the sum of all background classes.

TABLE VIII. Correlation matrix from the maximum likelihood fit.

	Φ_B	c_0	c_1	c_2	a_0	a_1
Φ_B	1.000	-0.723	0.302	-0.168	0.028	-0.012
c_0	-0.723	1.000	-0.299	-0.366	-0.376	0.129
c_1	0.302	-0.299	1.000	-0.206	0.219	-0.677
c_2	-0.168	-0.366	-0.206	1.000	0.008	-0.035
a_0	0.028	-0.376	0.219	0.008	1.000	-0.297
a_1	-0.012	0.129	-0.677	-0.035	-0.297	1.000

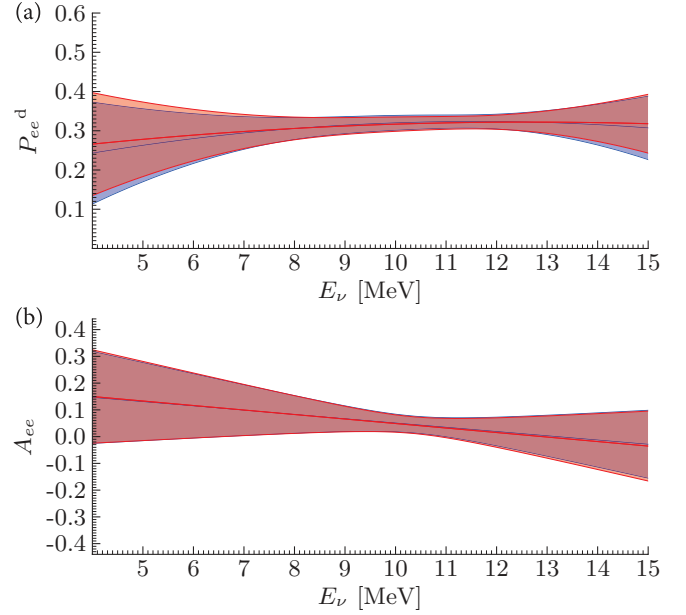


FIG. 10. (Color) rms spread in $P_{ee}^d(E_\nu)$ and $A_{ee}(E_\nu)$, taking into account the parameter uncertainties and correlations. The red band represents the results from the maximum likelihood fit, and the blue band represents the results from the Bayesian fit. The red and blue solid lines, respectively, are the best fits from the maximum likelihood and Bayesian fits.

VI. NEUTRINO OSCILLATIONS

Solar models predict the fluxes of neutrinos at the Earth, but the flavors of those neutrinos depends on the neutrino oscillation parameters and the details of where the neutrinos were produced in the Sun. Section VIA describes how the flavor components of the neutrino fluxes were calculated, and Sec. VIB describes how these predictions were compared to results for Φ_B , $P_{ee}^d(E_\nu)$, and $A_{ee}(E_\nu)$ presented here, and with other solar neutrino experiments. Reference [35] provides further details on the neutrino oscillation analysis presented here.

We considered two different neutrino oscillation hypotheses in this analysis. For comparison with previous SNO analyses, Sec. VIC presents the so-called two-flavor neutrino oscillations, which assumed $\theta_{13} = 0$ and had two free neutrino oscillation parameters, θ_{12} , and Δm_{21}^2 . In Sec. VID we also considered the so-called three-flavor neutrino oscillations, which had the following three free neutrino oscillation parameters: θ_{12} , θ_{13} , and Δm_{21}^2 . Note that the mixing angle, θ_{23} , and the CP-violating phase, δ , are irrelevant for the neutrino oscillation analysis of solar neutrino data. The solar neutrino data considered here was insensitive to the exact value Δm_{31}^2 , so we used a fixed value of $\pm 2.45 \times 10^3 \text{ eV}^2$ obtained from long-baseline accelerator experiments and atmospheric neutrino experiments [36].

A. Solar neutrino predictions

Predicting the solar neutrino flux and E_ν spectrum for all neutrino flavors requires a model of the neutrino production

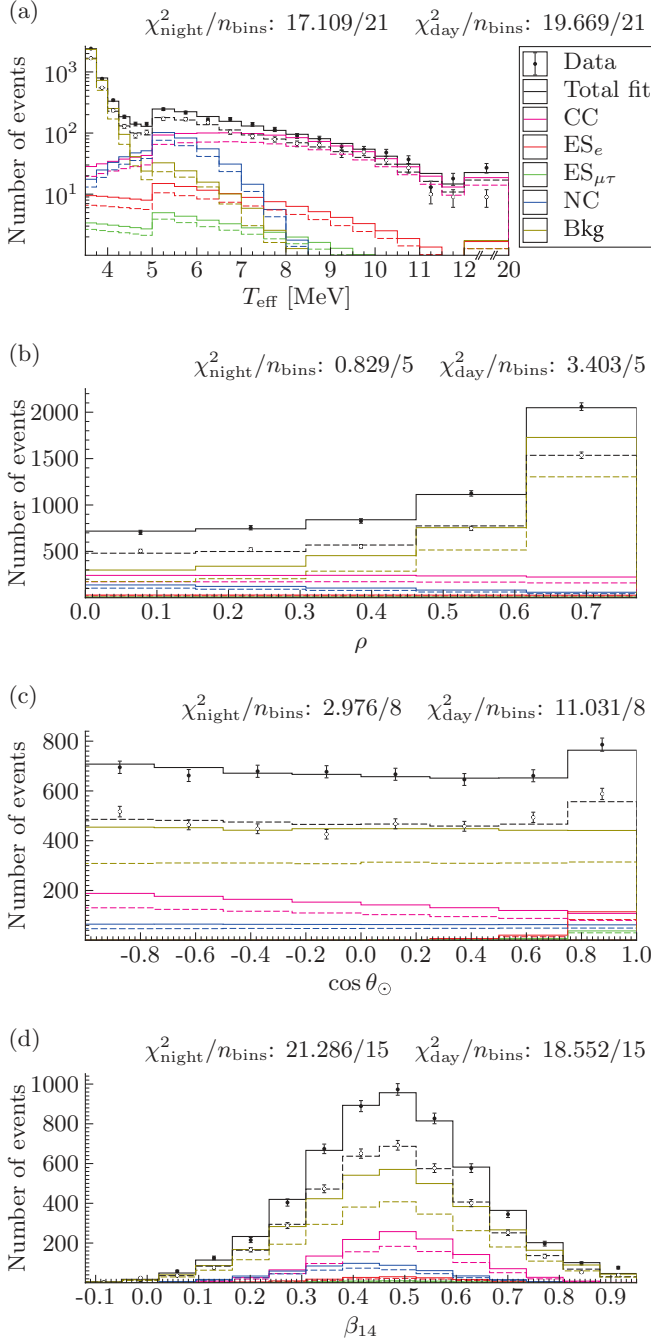


FIG. 11. (Color) Projection of the T_{eff} , ρ , $\cos \theta_{\odot}$, and β_{14} for the Phase I data. Day events hollow circles and dashed lines. Night events filled circle and solid lines. Note that the sharp break in the data in (a) at 5 MeV arises from change of bin width.

rates as a function of location within the Sun, and a model of the neutrino survival probabilities as they propagate through the Sun, travel to the Earth, and then propagate through the Earth. For consistency with previous calculations, and because of the conservative model uncertainties, we used the BS05(OP) model [22] to predict the solar neutrino production rate within the Sun rather than the more recent BPS09(GS) or BPS09(AGSS09) models [6]. Reference [35] provides the

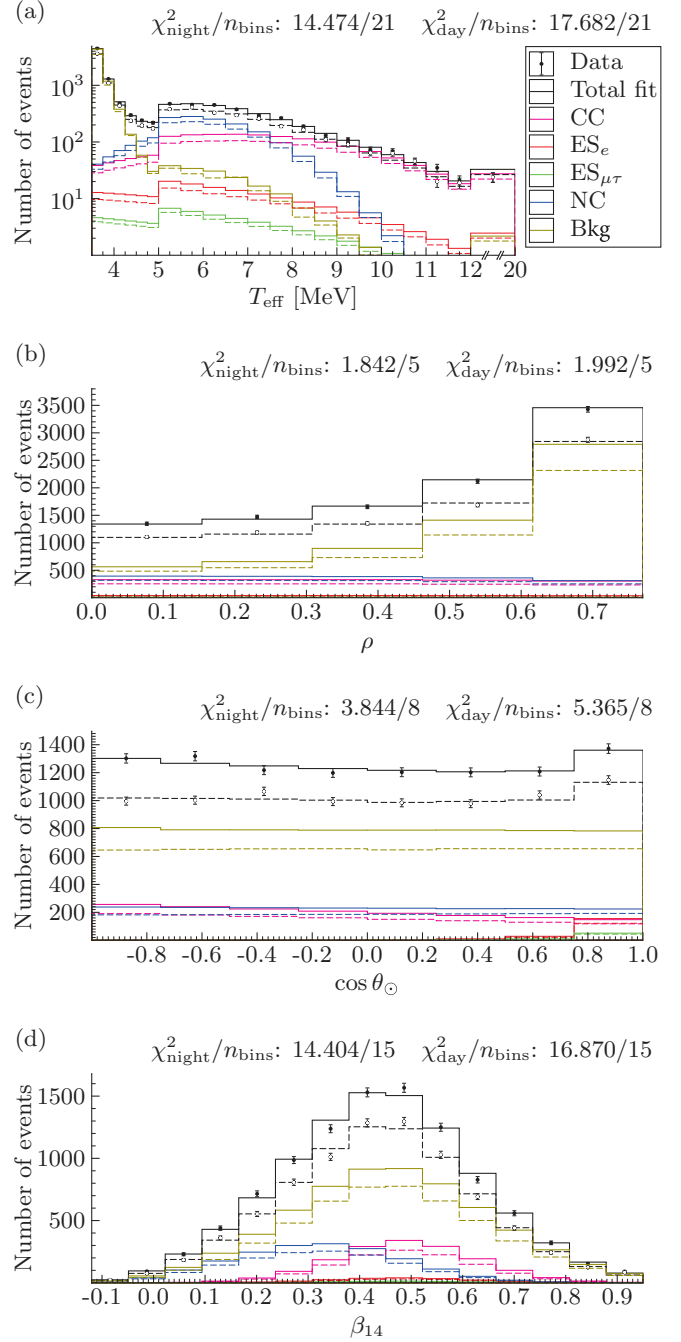


FIG. 12. (Color) Projection of the T_{eff} , ρ , $\cos \theta_{\odot}$, and β_{14} for the Phase II data. Day events hollow circles and dashed lines. Night events filled circle and solid lines. Note that the sharp break in the data in (a) at 5 MeV arises from change of bin width.

results presented below assuming these other solar models. We used the E_{ν} spectrum for ^8B neutrinos from Ref. [27], and all other spectra were from Ref. [37].

In previous analyses we used numerical calculations to construct a lookup table of neutrino survival probability as a function of the neutrino oscillation parameters. Such a table was still used to study the entire region of neutrino oscillation parameters. Previous analyses of SNO data combined with

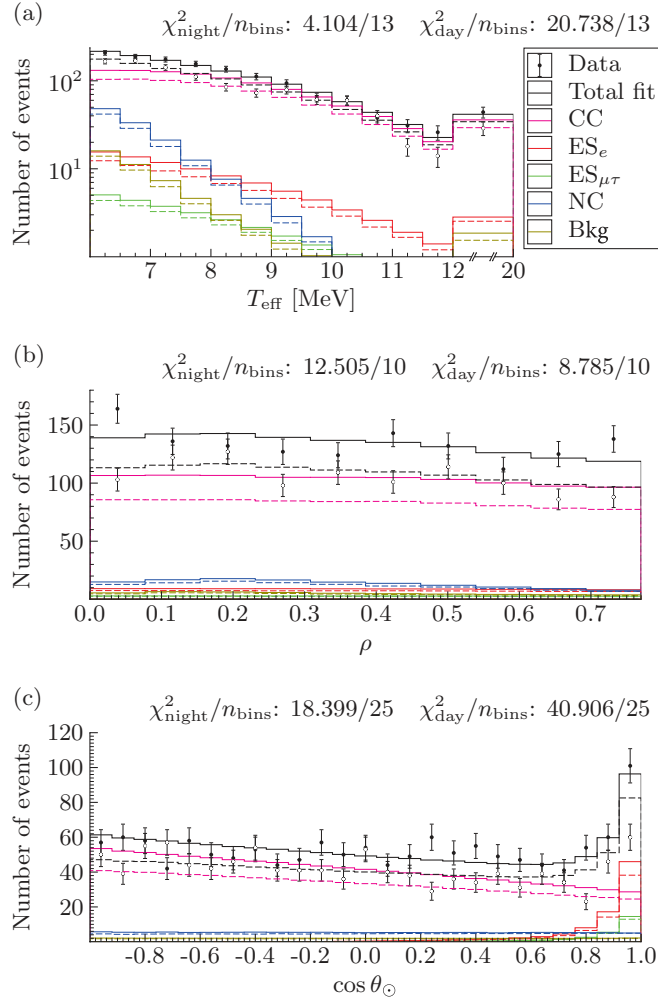


FIG. 13. (Color) Projection of the T_{eff} , ρ , and $\cos \theta_{\odot}$ for the data from Phase III. Day events hollow circles and dashed lines. Night events filled circle and solid lines.

other solar neutrino experiments left only the region referred to as LMA. This analysis used an adiabatic approximation when calculating neutrino oscillation parameters in that region. We verified that these two calculations gave equivalent results for a fixed set of neutrino oscillation parameters in the LMA region. Due to the improved speed of the adiabatic calculation we could scan discrete values of both Δm_{21}^2 and E_ν , whereas the lookup table used previously was calculated at discrete values of $\Delta m_{21}^2/E_\nu$, which resulted in small but observable discontinuities.

We also updated the electron density as a function of Earth radius, which affects the survival probability of neutrinos propagating through the Earth. Previous SNO analyses used the PREM [38] model, which averages over the continental and oceanic crust. When neutrinos enter the SNO detector from above they must have propagated through continental crust; therefore, we modified the Earth density profile to use PEM-C [39], which assumes continental crust for the outer most layer of the Earth. Because this significantly affected neutrinos only

during a short period of each day, this had a negligible effect on the calculated neutrino survival probability.

B. Analysis of solar neutrino and KamLAND data

To compare the ν_e survival probability parameters calculated in Sec. V with a neutrino oscillation prediction it was necessary to account for the sensitivity of the SNO detector. Table XXIII in Appendix D gives $S(E_\nu)$, the predicted spectrum of E_ν detectable by the SNO detector after including all effects such as the energy dependence of the cross sections, reaction thresholds, and analysis cuts, but not including neutrino oscillations. We multiplied $S(E_\nu)$ by the predicted neutrino oscillation hypothesis distortions, and fitted the resulting spectrum to $S(E_\nu)$ distorted by Eqs. (6) and (7). We then calculated the χ^2 between the results from this fit and our fit to the SNO data presented in Sec. VB. This calculation used the uncertainties and correlation matrix from the fit to SNO data, but did not include the uncertainties from the fit to the distorted $S(E_\nu)$ as this does not represent a measurement uncertainty.

The χ^2 was calculated as a function of the neutrino oscillation parameters. The best fit was determined from the parameters resulting in the minimum χ^2 , and the uncertainties were calculated from the change in χ^2 from this minimum. Tests with simulated data revealed that this method produced neutrino oscillation parameters that were unbiased and produced uncertainties consistent with frequentist statistics.

The following additional solar neutrino results were used in calculating the results from solar neutrino experiments: the solar neutrino rates measured in Ga [40] and Cl [41] experiments, the rate of ^7Be solar neutrinos measured in Borexino [42], and the rates and recoil electron energy spectra of ^8B neutrino ES reactions measured in Borexino [43], SuperKamiokande-I [44], SuperKamiokande-II [45], and SuperKamiokande-III [46]. The last two SuperKamiokande results were split into day and night, and the first SuperKamiokande result was split into multiple periods of the day. The difference in the day and night rate of ^7Be solar neutrinos recently measured in Borexino [47], and the recent measurement of the ^8B neutrino spectrum in KamLAND [48], were not included, but these results would not significantly change the results reported here. For a given set of neutrino oscillation parameters and Φ_B , the predictions for the set of experiments were calculated and compared to their results. This comparison was added to the χ^2 described above, and the resulting χ^2 was then minimized with respect to Φ_B . The same procedure as above was used to determine the best fit values and uncertainties.

The KamLAND experiment observed neutrino oscillations in $\bar{\nu}_e$ s from nuclear reactors. By assuming CPT invariance we can directly compare these results with the neutrino oscillations observed with solar neutrinos. Because this was a completely independent result, the lookup table of χ^2 as a function of θ_{12} , θ_{13} , and Δm_{21}^2 published by the KamLAND collaboration [49] was added directly to the χ^2 values calculated from the solar neutrino analysis, and the same procedure was used to determine the best fit values and uncertainties. The KamLAND result used in this analysis came directly

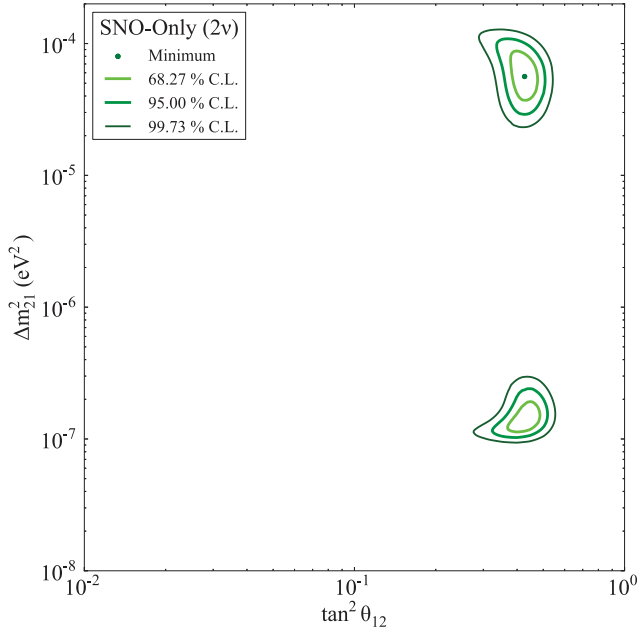


FIG. 14. (Color online) Two-flavor neutrino oscillation analysis contour using only SNO data.

from the KamLAND collaboration, and did not include an approximately 3% decrease in the expected neutrino flux from nuclear reactors due to a recent reevaluation of electron spectra from neutron activation of nuclear fusion isotopes [50]. Analysis of the KamLAND data by others [36,51] suggested that inclusion of this could change the constraints on θ_{13} .

C. Two-flavor neutrino oscillation analysis

Figure 14 shows the allowed regions of the $(\tan^2 \theta_{12}, \Delta m^2_{21})$ parameter space obtained with the results in Tables VII and VIII. SNO data alone cannot distinguish between the upper (LMA) region, and the lower (LOW) region, although it slightly favors the LMA region.

Figure 15 shows the allowed regions of the $(\tan^2 \theta_{12}, \Delta m^2_{21})$ parameter space obtained when the SNO results were combined with the other solar neutrino experimental results, and when this combined solar neutrino result was combined with the results from the KamLAND (KL) experiment. The combination of the SNO results with the other solar neutrino experimental results eliminates the LOW region, and eliminates the higher values of Δm^2_{21} in the LMA region. Table IX summarizes the results from these two-flavor neutrino analyses.

D. Three-flavor neutrino oscillation analysis

Recent results from the Daya Bay [52], RENO [53], and Double Chooz [54] short-baseline (SBL) reactor experiments confirmed a non-zero value of $\sin^2 \theta_{13}$. Because the SBL analyses were insensitive to θ_{12} , and because the solar neutrino plus KamLAND analysis was insensitive to Δm^2_{31} , the projections of $\Delta \chi^2$ onto θ_{13} can simply be added. Table X shows the results

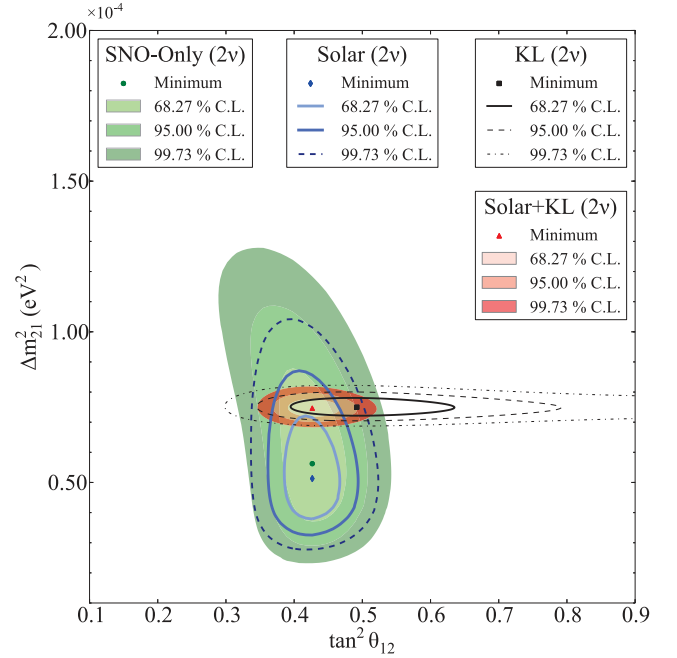


FIG. 15. (Color) Two-flavor neutrino oscillation analysis contour using both solar neutrino and KamLAND (KL) results.

of that combination. Other measurements from the T2K [55], MINOS [56] and CHOOZ [57] experiments were not included, but these results would not change significantly the results reported here.

Figure 16 shows the allowed regions of the $(\tan^2 \theta_{12}, \Delta m^2_{21})$ and $(\tan^2 \theta_{12}, \sin^2 \theta_{13})$ parameter spaces obtained from the results of all solar neutrino experiments as well as from the results of the KamLAND experiment. It also shows the result of the solar experiments combined with the results of the KamLAND experiment (Solar + KL) together with the combined results of the solar, KamLAND and SBL experiments (Sol + KL + SBL). Compared to the result in Fig. 15, this clearly shows that allowing nonzero values of θ_{13} brings the solar neutrino experimental results into better agreement with the results from the KamLAND experiment. Furthermore, a definite nonzero value of θ_{13} helped better determine θ_{12} in a three-flavor neutrino oscillation analysis.

Figure 17 shows the projection of these results onto the individual oscillation parameters. This result shows that due to the different dependence between $\tan^2 \theta_{12}$ and $\sin^2 \theta_{13}$ for

TABLE IX. Best-fit neutrino oscillation parameters from a two-flavor neutrino oscillation analysis. Uncertainties listed are $\pm 1\sigma$ after the χ^2 was minimized with respect to all other parameters.

Oscillation analysis	$\tan^2 \theta_{12}$	$\Delta m^2_{21} [\text{eV}^2]$	χ^2/NDF
SNO only (LMA)	$0.427^{+0.033}_{-0.029}$	$5.62^{+1.92}_{-1.36} \times 10^{-5}$	1.39/3
SNO only (LOW)	$0.427^{+0.043}_{-0.035}$	$1.35^{+0.35}_{-0.14} \times 10^{-7}$	1.41/3
Solar	$0.427^{+0.028}_{-0.028}$	$5.13^{+1.29}_{-0.96} \times 10^{-5}$	108.07/129
Solar + KamLAND	$0.427^{+0.027}_{-0.024}$	$7.46^{+0.20}_{-0.19} \times 10^{-5}$	

TABLE X. Best-fit neutrino oscillation parameters from a three-flavor neutrino oscillation analysis. Uncertainties listed are $\pm 1\sigma$ after the χ^2 was minimized with respect to all other parameters. The global analysis includes Solar + KL + SBL.

Analysis	$\tan^2 \theta_{12}$	$\Delta m_{21}^2 [\text{eV}^2]$	$\sin^2 \theta_{13} (\times 10^{-2})$
Solar	$0.436^{+0.048}_{-0.036}$	$5.13^{+1.49}_{-0.98} \times 10^{-5}$	< 5.8 (95% C.L.)
Solar + KL	$0.443^{+0.033}_{-0.026}$	$7.46^{+0.20}_{-0.19} \times 10^{-5}$	$2.5^{+1.8}_{-1.4}$
Solar + KL + SBL	$0.443^{+0.030}_{-0.025}$	$7.46^{+0.20}_{-0.19} \times 10^{-5}$	< 5.3 (95% C.L.)

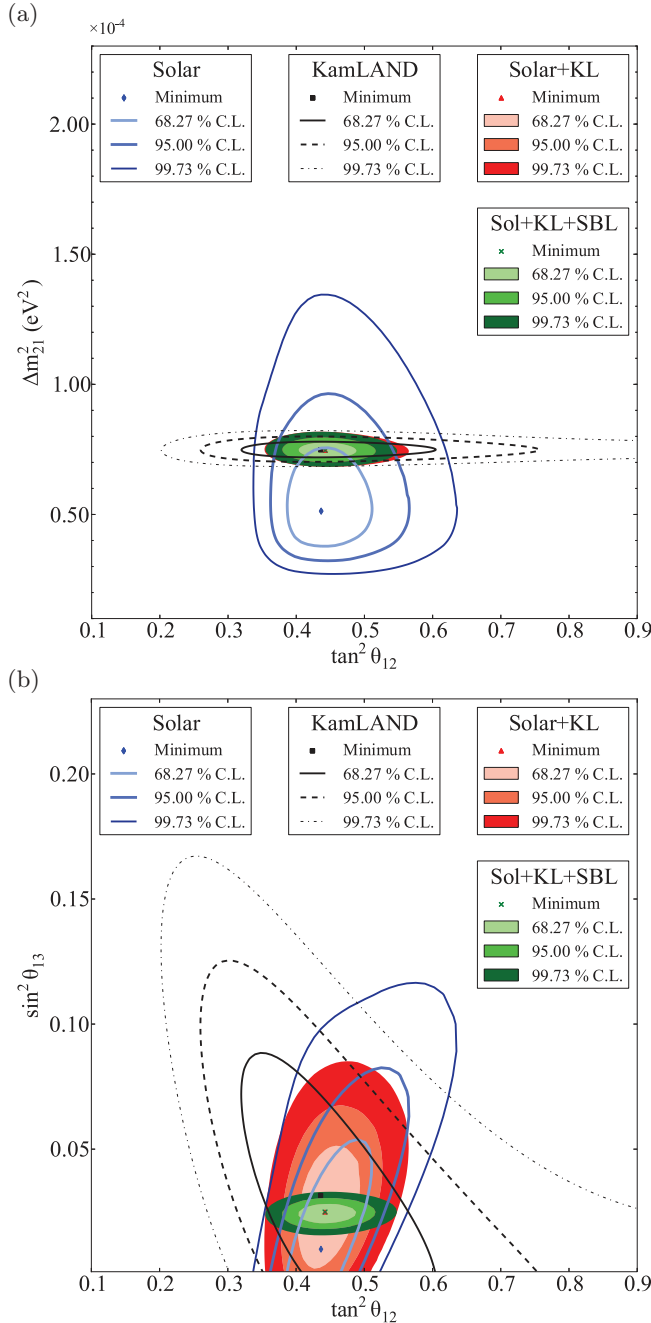


FIG. 16. (Color) Three-flavor neutrino oscillation analysis contour using the solar neutrino, KamLAND (KL), and SBL results.

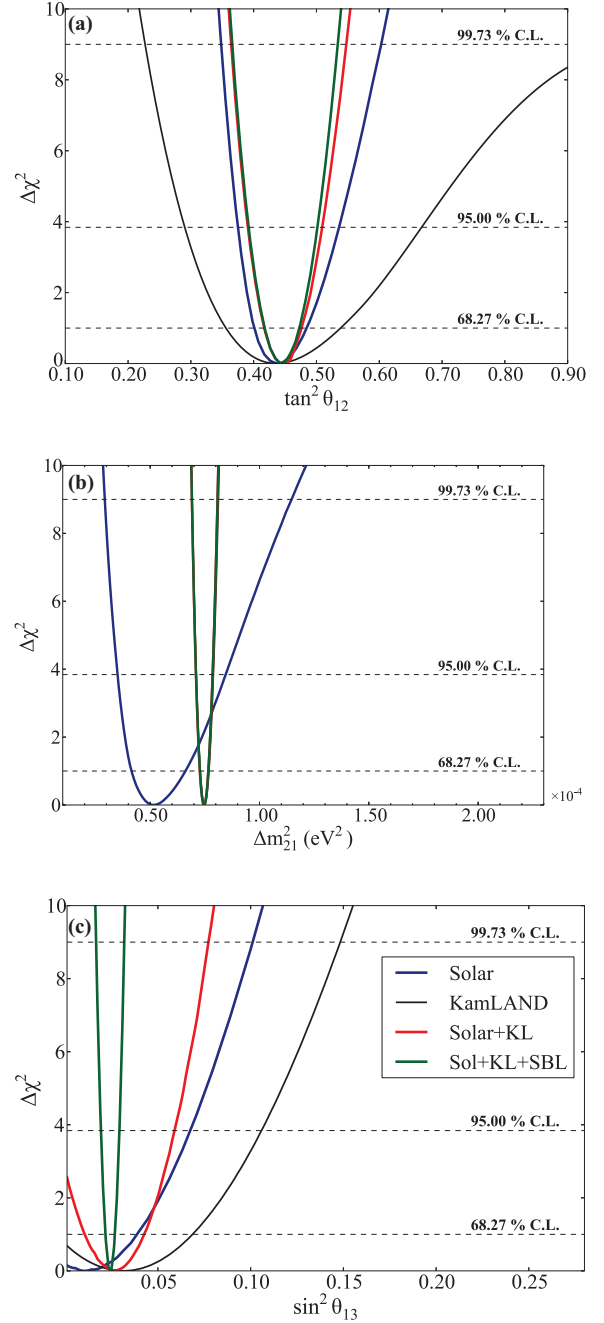


FIG. 17. (Color) Projections of the three-flavor neutrino oscillation parameters determined from Fig. 16. The horizontal lines representing the $\Delta\chi^2$ for a particular confidence level are for two-sided intervals. Note, in (b) the KamLAND, Solar + KL, and Sol + KL + SBL lines are on top of each other.

the solar neutrino experimental results and the KamLAND experimental results, the combined constraint on $\sin^2 \theta_{13}$ was better than the individual constraints.

Table X summarizes the results from these three-flavor neutrino oscillation analyses. Tests with the inverted hierarchy, i.e., negative values of Δm_{31}^2 , gave essentially identical results [35].

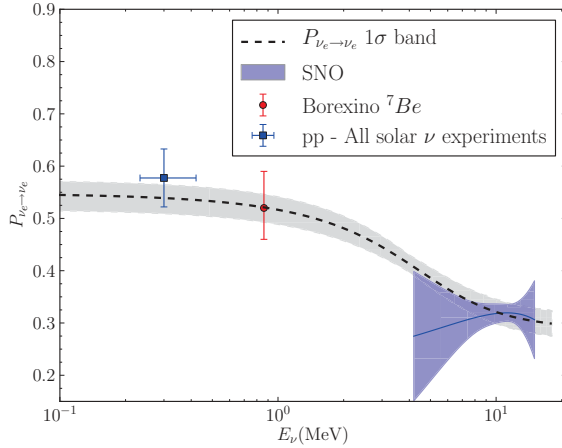


FIG. 18. (Color online) Various solar ν_e survival probability measurements compared to the LMA prediction for ^8B neutrino. Using the results from Sec. VI of this paper, the dashed line is the best fit LMA solution for ^8B neutrinos and the gray shaded band is the 1σ uncertainty. The corresponding bands for ν_e s from the pp and ^7Be reactions (not shown) are almost identical in the region of those measurements. The blue shaded band is the result of the measurement of the ^8B neutrino ν_e survival probability reported here. The red point is the result of the Borexino measurement [42] of the survival probability for ν_e s produced by $^7\text{Be} + e^- \rightarrow ^7\text{Li} + \nu_e$ reactions in the Sun. The blue point is the result of various measurements [40] of the survival probability for ν_e s produced by $p + p \rightarrow ^2\text{H} + e^+ + \nu_e$ reactions in the Sun; note that these measurements did not exclusively measure this reaction, so the contribution from other reactions were removed assuming the best fit LMA solution, and so actually depends on all solar neutrino results. The uncertainty in absolute flux of the subtracted reactions was included in the calculation of the total uncertainty of this point, but the uncertainty due to the neutrino oscillation probability of these reactions was not. The uncertainty due to the normalization of the two points by the expected flux was included. For clarity, this plot illustrates the LMA solution relative to only a subset of the solar neutrino experimental results.

Figure 18 shows the measured solar ν_e survival probability as a function of E_ν . At higher E_ν the results of this analysis provide the best constraints on the survival probability. All solar results are consistent with the LMA neutrino oscillation hypothesis.

VII. DISCUSSION AND CONCLUSIONS

In this paper we include a new analysis of the data from Phase III of the experiment with particle identification to distinguish neutron waveforms from background α waveforms and we make improvements to the previous analysis of the first two phases of the experiment [7]. By performing a full analysis of the data for all three phases we correctly account for correlations in the systematic uncertainties and thereby provide the most complete analysis available for the full solar neutrino data from the SNO detector.

The new analysis of data from Phase III of the SNO experiment eliminated most of the background from α events

and allowed a very general PDF to describe the E_{NCD} spectrum for any remaining background events. This made the analysis less sensitive to background uncertainties than our previous analysis of these data.

Combining data from all phases of the SNO experiment we measured a total flux of active flavor neutrinos from ^8B decays in the Sun of $(5.25 \pm 0.16(\text{stat.})^{+0.11}_{-0.13}(\text{syst.})) \times 10^6 \text{ cm}^{-2}\text{s}^{-1}$. We improved the handling of a number of systematic uncertainties in this analysis compared with our previous analyses of these data. This result is consistent with but more precise than both the BPS09(GS), $(5.88 \pm 0.65) \times 10^6 \text{ cm}^{-2}\text{s}^{-1}$, and BPS09(AGSS09), $(4.85 \pm 0.58) \times 10^6 \text{ cm}^{-2}\text{s}^{-1}$, solar model predictions [6].

The precision of the ν_e survival probability parameters was improved by approximately 20% compared to our previously reported results due to the additional constraint provided by the data from Phase III. During the day the ν_e survival probability at 10 MeV was $c_0 = 0.317 \pm 0.016(\text{stat.}) \pm 0.009(\text{syst.})$, which was inconsistent with the null hypothesis at much greater than seven sigma that there were no neutrino oscillations. The null hypotheses that there were no spectral distortions of the ν_e survival probability (i.e., $c_1 = 0$, $c_2 = 0$, $a_0 = 0$, $a_1 = 0$), and that there were no day/night distortions of the ν_e survival probability (i.e. $a_0 = 0$, $a_1 = 0$) could not be rejected at the 95% C.L.

A two-flavor neutrino oscillation analysis using only SNO results yielded $\Delta m_{21}^2 = (5.6^{+1.9}_{-1.4}) \times 10^{-5} \text{ eV}^2$ and $\tan^2 \theta_{12} = 0.427^{+0.033}_{-0.029}$. A three-flavor neutrino oscillation analysis combining the SNO results with results of all other solar neutrino experiments and the KamLAND experiment yielded $\Delta m_{21}^2 = (7.46^{+0.20}_{-0.19}) \times 10^{-5} \text{ eV}^2$, $\tan^2 \theta_{12} = 0.443^{+0.033}_{-0.026}$, and $\sin^2 \theta_{13} = (2.5^{+1.8}_{-1.4}) \times 10^{-2}$. This implied an upper bound of $\sin^2 \theta_{13} < 0.053$ at the 95% C.L. A global three-flavor neutrino oscillation analysis combining solar neutrino and reactor experiments yielded $\Delta m_{21}^2 = (7.46^{+0.20}_{-0.19}) \times 10^{-5} \text{ eV}^2$, $\tan^2 \theta_{12} = 0.443^{+0.030}_{-0.025}$, and $\sin^2 \theta_{13} = (2.49^{+0.20}_{-0.32}) \times 10^{-2}$.

ACKNOWLEDGMENTS

This research was supported by Canada: Natural Sciences and Engineering Research Council, Industry Canada, National Research Council, Northern Ontario Heritage Fund, Atomic Energy of Canada, Ltd., Ontario Power Generation, High Performance Computing Virtual Laboratory, Canada Foundation for Innovation, Canada Research Chairs; US: Department of Energy, National Energy Research Scientific Computing Center, Alfred P. Sloan Foundation; UK: Science and Technology Facilities Council; Portugal: Fundação para a Ciência e a Tecnologia. We thank the SNO technical staff for their strong contributions. We thank Vale (formerly Inco, Ltd.) for hosting this project.

APPENDIX A: STERILE NEUTRINOS

If we assume a sterile neutrino, where the probability of an electron neutrino oscillating into a sterile neutrino, $P_{es}(E_\nu)$, was the same during the day and night, then the scaling

TABLE XI. ^8B neutrino interactions scaling factors including a probability of an electron neutrino oscillating into a sterile neutrino, which was the same during the day and night. $P_{ee}^n(E_\nu) = P_{ee}^d(E_\nu)^{\frac{2+A_{ee}(E_\nu)}{2-A_{ee}(E_\nu)}}$, and $f(E_\nu)$ was the predicted spectrum of E_ν detectable by the SNO detector after including the energy dependence of the cross section.

Interaction	Day/Night	Scaling factor
CC, ES _e	Day	$\Phi_B P_{ee}^d(E_\nu)$
ES _{$\mu\tau$}	Day	$\Phi_B[1 - P_{ee}^d(E_\nu) - P_{es}(E_\nu)]$
CC, ES _e	Night	$\Phi_B P_{ee}^n(E_\nu)$
ES _{$\mu\tau$}	Night	$\Phi_B[1 - P_{ee}^n(E_\nu) - P_{es}(E_\nu)]$
NC	Day + Night	$\Phi_B \frac{\int (1 - P_{es}(E_\nu)) f(E_\nu) dE_\nu}{\int f(E_\nu) dE_\nu}$

factors given in Table I of Sec. III A are replaced with those in Table XI.

If $P_{es}(E_\nu)$ was a constant as a function of E_ν , and defining $\Phi'_B = \Phi_B(1 - P_{es}(E_\nu))$, and $P_{ee}^d(E_\nu)' = \frac{P_{ee}^d(E_\nu)}{1 - P_{es}(E_\nu)}$ we obtain the scaling factors given in Table XII.

Notice that scaling factors in Table XII are equivalent to those in Table I, except our measurement of the ^8B neutrino flux would be the true flux scaled by $(1 - P_{es}(E_\nu))$ and our measurement of $P_{ee}^d(E_\nu)$ would be scaled by $1/(1 - P_{es}(E_\nu))$.

We note that the approximations made in this analysis were also valid for effects involving sterile neutrinos with spectral distortion that are significant only below about 4 MeV and with small day-night effects for the NC detection process. In this case the principal additional effect would be a further renormalization of the NC interaction rate.

APPENDIX B: ALTERNATIVE ANALYSIS

Table XIII shows the results from an alternative Bayesian analysis.

APPENDIX C: CONSTRAINTS ON THE LIKELIHOOD FIT

Systematic uncertainties were propagated on the PDFs as described in this section.

1. T_{eff} PDFs

Table XIV lists the systematic uncertainties on the PDFs of T_{eff} . For Phases I and II the modified T_{eff} , T'_{eff} , during the day

TABLE XII. ^8B neutrino interactions scaling factors. $P_{ee}^n(E_\nu)' = P_{ee}^d(E_\nu)' \frac{2+A_{ee}(E_\nu)}{2-A_{ee}(E_\nu)}$.

Interaction	Day/Night	Scaling factor
CC, ES _e	Day	$\Phi'_B P_{ee}^d(E_\nu)'$
ES _{$\mu\tau$}	Day	$\Phi'_B[1 - P_{ee}^d(E_\nu)']$
CC, ES _e	Night	$\Phi'_B P_{ee}^n(E_\nu)'$
ES _{$\mu\tau$}	Night	$\Phi'_B[1 - P_{ee}^n(E_\nu)']$
NC	Day + Night	Φ'_B

TABLE XIII. Results from the Bayesian fit. As this is a secondary analysis, we recommend using the results in Table VII. The numbers in this table are obtained from the mean and standard deviation of the posterior probability distribution using flat priors for Φ_B and the ν oscillation parameters. Note that Φ_B is in units of $\times 10^6 \text{ cm}^{-2} \text{ s}^{-1}$.

	Best fit	Total uncertainty
Φ_B	5.24	± 0.21
c_0	0.321	± 0.019
c_1	0.0043	± 0.0078
c_2	-0.0017	± 0.0034
a_0	0.049	± 0.034
a_1	-0.016	± 0.027

was obtained from

$$T'_{\text{eff}} = (1 + a_0^E + a_0^E - A_{dn}^E/2 - A_{dir}^E/2)T_{\text{eff}}. \quad (\text{C1})$$

The signs of the A_{dn}^E and A_{dir}^E terms were reversed for night. The uncertainty due to T_{eff} resolution was obtained by convolving T'_{eff} with Gaussians centered at zero with widths of σ^E , and σ_{dn}^E and σ_{dir}^E scaled by a parameterized detector resolution. This resolution was applied first to just day events and then to just night events. Differences in the neutrino parameters between the shifted fits and the central fit were taken as the resulting uncertainties.

During Phase III the modified T_{eff} , T''_{eff} , was obtained from

$$T''_{\text{eff}} = T'_{\text{eff}} + b_0^E(1 - B_{dir}^E/2)(T'_{\text{eff}} - T_g), \quad (\text{C2})$$

where T_g was the true MC energy. For the NC and external neutrons PDFs T_g was constant and equal to the mean fitter energy 5.65 MeV. T'_{eff} was obtained from

$$T'_{\text{eff}} = (1 + a_0^E + a_0^E)(1 - A_{dn}^E/2 - A_{dir}^E/2)T_{\text{eff}}, \quad (\text{C3})$$

where the signs of the A_{dn}^E and A_{dir}^E terms were reversed for night.

2. β_{14} PDFs

Table XV lists the systematic uncertainties on the PDFs of β_{14} . During the day these uncertainties were applied using

$$\beta'_{14} = \beta_{14}(1 + a_0^{\beta_{14}} + c_0^{\beta_{14}}(T_{\text{eff}} - 5.589[\text{MeV}])) - A_{dn}^{\beta_{14}}/2 - A_{dir}^{\beta_{14}}/2. \quad (\text{C4})$$

The signs of the $A_{dn}^{\beta_{14}}$ and $A_{dir}^{\beta_{14}}$ terms were reversed for night. For electrons and γ rays the systematic uncertainties associated with β_{14} resolution were applied as

$$\beta''_{14} = \beta'_{14} + (\beta'_{14} - \bar{\beta}_{14})b_0^{\beta_{14}}, \quad (\text{C5})$$

where β''_{14} was the value of β_{14} including all of the systematic uncertainties, and $\bar{\beta}_{14}$ a parameterized average value of β_{14} for the PDF. For neutrons in Phase II the systematic uncertainties associated with resolution were applied as a convolution with a Gaussian centered at zero with a width of $\sigma^{\beta_{14}}$. This correction can only be applied in the positive direction, and the negative fit uncertainties were inferred to be the same as the positive ones.

TABLE XIV. T_{eff} PDF systematic uncertainties.

Parameter	Description	Events	Phase	Nominal	Variation	Fit value	Application
a_{0c}^E	T_{eff} scale	all	I, II, III	0	± 0.0041	$0.0004^{+0.0033}_{-0.0024}$	scanned
a_0^E	T_{eff} scale	all	I	0	$^{+0.0039}_{-0.0047}$	$-0.0007^{+0.0038}_{-0.0030}$	scanned
a_0^E	T_{eff} scale	all	II	0	$^{+0.0034}_{-0.0032}$	$0.0001^{+0.0026}_{-0.0027}$	scanned
a_0^E	T_{eff} scale	all	III	0	± 0.0081	$0.0065^{+0.0042}_{-0.0084}$	scanned
c_0^E	T_{eff} scale nonlinearity with T_{eff}	all	I, II, III	0	± 0.0069	N/A	shift-and-refit
A_{dn}^E	T_{eff} scale diurnal variation	all	I	0	± 0.0032	N/A	shift-and-refit
A_{dir}^E	T_{eff} scale directional variation	CC	I	0	$\pm 0.0009^a$	N/A	shift-and-refit
A_{dir}^E	T_{eff} scale directional variation	ES	I	0	$\pm 0.0092^a$	N/A	N/A
A_{dn}^E	T_{eff} scale diurnal variation	all	II	0	± 0.004	N/A	shift-and-refit
A_{dir}^E	T_{eff} scale directional variation	CC	II	0	$\pm 0.0009^b$	N/A	shift-and-refit
A_{dir}^E	T_{eff} scale directional variation	ES	II	0	$\pm 0.0079^b$	N/A	N/A
A_{dn}^E	T_{eff} scale diurnal variation	all	III	0	± 0.0038	$0.0005^{+0.0037}_{-0.0035}$	scanned
A_{dir}^E	T_{eff} scale directional variation	ES	III	0	± 0.0099	$-0.0038^{+0.0099}_{-0.0096}$	scanned
σ^E [MeV]	T_{eff} resolution	all	I	0.155	$^{+0.041}_{-0.080}$	$0.214^{+0.023}_{-0.034}$	scanned
σ^E [MeV]	T_{eff} resolution	e^-, γ	II	0.168	$^{+0.041}_{-0.080}$	$0.203^{+0.033}_{-0.041}$	scanned
σ^E [MeV]	T_{eff} resolution	n	II	0.154	± 0.018	$0.155^{+0.017}_{-0.019}$	scanned
b_0^E	T_{eff} resolution	n	III	0.0119	$\pm 0.0104^c$	$0.0109^{+0.0107}_{-0.0100}$	scanned
b_0^E	T_{eff} resolution	e^-, γ	III	0.016184	$\pm 0.0141^c$	N/A	N/A
σ_{dn}^E	T_{eff} resolution diurnal variation	all	I	0	± 0.003	N/A	shift-and-refit
σ_{dir}^E	T_{eff} resolution directional variation	CC	I	0	$\pm 0.0014^d$	N/A	shift-and-refit
σ_{dir}^E	T_{eff} resolution directional variation	ES	I	0	$\pm 0.0064^d$	N/A	N/A
σ_{dn}^E	T_{eff} resolution diurnal variation	all	II	0	± 0.005	N/A	shift-and-refit
σ_{dir}^E	T_{eff} resolution directional variation	CC	II	0	$\pm 0.0013^e$	N/A	shift-and-refit
σ_{dir}^E	T_{eff} resolution directional variation	ES	II	0	$\pm 0.013^e$	N/A	N/A
B_{dir}^E	T_{eff} resolution directional variation	ES	III	0	± 0.012	0.000 ± 0.012	scanned

^aCorrelation of -1 .^bCorrelation of -1 .^cCorrelation of 1 .^dCorrelation of -1 .^eCorrelation of -1 .TABLE XV. β_{14} PDF systematic uncertainties.

Parameter	Description	Events	Phase	Nominal	Variation	Fit value	Application
a_0^β	β_{14} scale	all	I	-0.0081	$\pm 0.0042^a$	N/A	scanned
a_0^β	β_{14} scale	e^-	II	0	$\pm 0.0024^a$	$0.00102^{+0.00112}_{-0.00205}$	N/A
a_0^β	β_{14} scale	n	II	-0.0144	$^{+0.0038}_{-0.0022}$	$-0.0138^{+0.0036}_{-0.0025}$	scanned
c_0^β	β_{14} scale nonlinearity with T_{eff}	all	I, II	0.00275597	± 0.00069	$0.00201^{+0.00058}_{-0.00044}$	scanned
A_{dn}^β	β_{14} offset diurnal variation	all	I	0	± 0.0043	N/A	shift-and-refit
A_{dir}^β	β_{14} offset directional variation	CC	I	0	$\pm 0.00038^b$	N/A	shift-and-refit
A_{dir}^β	β_{14} offset directional variation	ES	I	0	$\pm 0.0034^b$	N/A	N/A
A_{dn}^β	β_{14} offset diurnal variation	all	II	0	± 0.0043	N/A	shift-and-refit
A_{dir}^β	β_{14} offset directional variation	CC	II	0	$\pm 0.00038^c$	N/A	shift-and-refit
A_{dir}^β	β_{14} offset directional variation	ES	II	0	$\pm 0.0034^c$	N/A	N/A
b_0^β	β_{14} resolution	all	I	0	$\pm 0.0042^d$	N/A	shift-and-refit
b_0^β	β_{14} resolution	e^-	II	0	$\pm 0.0054^d$	N/A	N/A
σ^β	β_{14} resolution	n	II	0.0150	± 0.0045	N/A	shift-and-refit

^aCorrelation of 1 .^bCorrelation of -1 .^cCorrelation of -1 .^dCorrelation of 1 .

TABLE XVI. ρ PDF systematic uncertainties.

Parameter	Description	Events	Phase	Nominal	Variation	Fit value	Application
a_1^ρ	ρ scale	all	I	0	+0.0010 -0.0057	N/A	shift-and-refit
a_1^z	z scale	all	I	0	+0.0040 -0.0	N/A	shift-and-refit
a_1^ρ	ρ scale	all	II	0	+0.0004 -0.0034	N/A	shift-and-refit
a_1^z	z scale	all	II	0	+0.0003 -0.0025	N/A	shift-and-refit
a_1^ρ	ρ scale	all	III	0	+0.0029 -0.0077	$0.0004^{+0.0027}_{-0.0051}$	scanned
a_1^z	z scale	all	III	0	+0.0015 -0.0012	N/A	shift-and-refit
c^ρ	ρ scale nonlinearity with T_{eff}	all	I	0	+0.0085 -0.0049	N/A	shift-and-refit
c^ρ	ρ scale nonlinearity with T_{eff}	all	II	0	+0.0041 -0.0048	N/A	shift-and-refit
c^ρ	ρ scale nonlinearity with T_{eff}	all	III	0	+0.0088 -0.0067	N/A	shift-and-refit
A_{dn}^ρ	ρ scale diurnal variation	all	I	0	± 0.002	N/A	shift-and-refit
A_{dir}^ρ	ρ scale directional variation	CC	I	0	$\pm 0.0004^a$	N/A	shift-and-refit
A_{dir}^ρ	ρ scale directional variation	ES	I	0	$\pm 0.005^a$	N/A	N/A
A_{dn}^ρ	ρ scale diurnal variation	all	II	0	± 0.003	N/A	shift-and-refit
A_{dir}^ρ	ρ scale directional variation	CC	II	0	$\pm 0.0002^b$	N/A	shift-and-refit
A_{dir}^ρ	ρ scale directional variation	ES	II	0	$\pm 0.0015^b$	N/A	N/A
A_{dn}^ρ	ρ scale diurnal variation	all	III	0	± 0.0015	N/A	shift-and-refit
A_{dir}^ρ	ρ scale directional variation	ES	III	0	± 0.0018	N/A	shift-and-refit
a_0^x [cm]	x shift	all	I	0	+1.15 -0.13	N/A	shift-and-refit
a_0^y [cm]	y shift	all	I	0	+2.87 -0.17	N/A	shift-and-refit
a_0^z [cm]	z shift	all	I	5	+2.58 -0.15	N/A	shift-and-refit
a_0^x [cm]	x shift	all	II	0	+0.62 -0.07	N/A	shift-and-refit
a_0^y [cm]	y shift	all	II	0	+2.29 -0.09	N/A	shift-and-refit
a_0^z [cm]	z shift	all	II	5	+3.11 -0.16	N/A	shift-and-refit
a_0^x [cm]	x shift	all	III	0	± 4.0	N/A	shift-and-refit
a_0^y [cm]	y shift	all	III	0	± 4.0	N/A	shift-and-refit
a_0^z [cm]	z shift	all	III	5	± 4.0	N/A	shift-and-refit
σ^x [cm]	x resolution	all	I	0	± 3.3	N/A	shift-and-refit
σ^y [cm]	y resolution	all	I	0	± 2.2	N/A	shift-and-refit
σ^z [cm]	z resolution	all	I	0	± 1.5	N/A	shift-and-refit
σ^x [cm]	x resolution	all	II	0	± 3.1	N/A	shift-and-refit
σ^y [cm]	y resolution	all	II	0	± 3.4	N/A	shift-and-refit
σ^z [cm]	z resolution	all	II	0	± 5.3	N/A	shift-and-refit
$b_0^{x,y}$	x, y resolution constant term	all	III	0.065	$\pm 0.029^c$	N/A	shift-and-refit
$b_1^{x,y}$ [cm $^{-1}$]	x, y resolution linear term	all	III	-5.5×10^{-5}	$\pm 6.1 \times 10^{-5c}$	N/A	shift-and-refit
$b_2^{x,y}$ [cm $^{-2}$]	x, y resolution quadratic term	all	III	3.9×10^{-7}	$\pm 2.0 \times 10^{-7c}$	N/A	shift-and-refit
b_0^z	z resolution constant term	all	III	0.0710	$\pm 0.028^d$	N/A	shift-and-refit
b_1^z [cm $^{-1}$]	z resolution linear term	all	III	1.16×10^{-4}	$\pm 0.83 \times 10^{-4d}$	N/A	shift-and-refit
σ_{dn}^ρ [cm]	ρ resolution diurnal variation	all	I	0	± 6.82	N/A	shift-and-refit
σ_{dn}^ρ [cm]	ρ resolution diurnal variation	all	II	0	± 7.21	N/A	shift-and-refit
σ_{dir}^ρ [cm]	ρ resolution directional variation	CC	II	0	$\pm 1.02^e$	N/A	shift-and-refit
σ_{dir}^ρ [cm]	ρ resolution directional variation	ES	II	0	$\pm 3.36^e$	N/A	N/A

^aCorrelation of -1 .^bCorrelation of $\begin{pmatrix} 1 & -0.13 & -0.74 \\ -0.13 & 1 & 0.31 \\ -0.74 & 0.31 & 1 \end{pmatrix}$.^cCorrelation of 0.15.^dCorrelation of 0.15.^eCorrelation of -1 .

3. ρ PDFs

Table XVI lists the systematic uncertainties on the PDFs of ρ . The radius was modified by

$$\rho'' = \frac{[(x''[\text{cm}])^2 + (y''[\text{cm}])^2 + (z''[\text{cm}])^2]^{3/2}}{600^3}, \quad (\text{C6})$$

where x'' , y'' , and z'' were the modified Cartesian coordinates, as described below. Each event was weighted by a factor $1 + c^\rho \times (T_{\text{eff}} - 5.05[\text{MeV}])$.

During Phases I and II, x'' , y'' , and z'' , respectively, were obtained by convolving x' , y' , and z' with Gaussians centered at zero with widths of σ^x , σ^y , σ^z , σ_{dn}^ρ , or σ_{dir}^ρ . These resolutions

TABLE XVII. $\cos \theta_\odot$ PDF systematic uncertainties.

Parameter	Description	Events	Phase	Nominal	Variation	Fit value	Application
a_0^θ	$\cos \theta_\odot$ scale	ES	I	0	± 0.11	N/A	shift-and-refit
a_0^θ	$\cos \theta_\odot$ scale	ES	II	0	± 0.11	N/A	shift-and-refit
a_0^θ	$\cos \theta_\odot$ scale	ES	III	0	± 0.12	$0.063^{+0.104}_{-0.099}$	scanned
A_{dir}^θ	$\cos \theta_\odot$ scale directional variation	ES	I	0	± 0.022	N/A	shift-and-refit
A_{dir}^θ	$\cos \theta_\odot$ scale directional variation	ES	II	0	± 0.052	N/A	shift-and-refit
A_{dir}^θ	$\cos \theta_\odot$ scale directional variation	ES	III	0	± 0.069	$-0.015^{+0.073}_{-0.066}$	scanned

were applied first to only day events and then to only night events. x' , y' , and z' were obtained from

$$x' = (1 + a_1^\rho - A_{dn}^\rho/2 - A_{\text{dir}}^\rho/2)(x + a_0^x), \quad (\text{C7})$$

$$y' = (1 + a_1^\rho - A_{dn}^\rho/2 - A_{\text{dir}}^\rho/2)(y + a_0^y), \quad (\text{C8})$$

$$z' = (1 + a_1^\rho + a_1^z - A_{dn}^\rho/2 - A_{\text{dir}}^\rho/2)(z + a_0^z). \quad (\text{C9})$$

The signs of the A_{dn}^ρ and A_{dir}^ρ terms were reversed for night.

During Phase III the uncertainties were applied as

$$x'' = x' + (b_0^{x,y} + b_1^{x,y}z + b_2^{x,y}z^2)(x' - x_g), \quad (\text{C10})$$

$$y'' = y' + (b_0^{x,y} + b_1^{x,y}z + b_2^{x,y}z^2)(y' - y_g), \quad (\text{C11})$$

$$z'' = z' + (b_0^z + b_1^z z)(z' - z_g), \quad (\text{C12})$$

where x_g , y_g , z_g were the true MC positions. x' , y' , and z' were obtained from

$$x' = (1 + a_1^\rho)(1 - A_{dn}/2 - A_{\text{dir}}/2)(x + a_0^x), \quad (\text{C13})$$

$$y' = (1 + a_1^\rho)(1 - A_{dn}/2 - A_{\text{dir}}/2)(y + a_0^y), \quad (\text{C14})$$

$$z' = (1 + a_1^\rho + a_1^z)(1 - A_{dn}/2 - A_{\text{dir}}/2)(z + a_0^z). \quad (\text{C15})$$

The signs of the A_{dn}^ρ and A_{dir}^ρ terms were reversed for night.

4. $\cos \theta_\odot$ PDFs

Table XVII lists the systematic uncertainties on the PDFs of $\cos \theta_\odot$. For Phases I and II the modified $\cos \theta_\odot$, $\cos \theta'_\odot$, was obtained from

$$\cos \theta'_\odot = 1 + (1 + a_0^\theta - A_{\text{dir}}^\theta/2)(\cos \theta_\odot - 1). \quad (\text{C16})$$

For Phase III the modified $\cos \theta_\odot$, $\cos \theta'_\odot$, was obtained from

$$\cos \theta'_\odot = 1 + (1 + a_0^\theta)(1 - A_{\text{dir}}^\theta/2)(\cos \theta_\odot - 1). \quad (\text{C17})$$

TABLE XVIII. E_{NCD} PDF systematic uncertainties.

Parameter	Description	Events	Phase	Nominal	Variation
$a_1^{E_{\text{NCD}}}$	E_{NCD} scale	n	III	0	± 0.01
$b_0^{E_{\text{NCD}}}$	E_{NCD} resolution	n	III	0	$^{+0.01}_{-0.00}$

If the transformation moved $\cos \theta'_\odot$ outside the range $[-1, 1]$, $\cos \theta'_\odot$ was given a random value within this interval.

5. E_{NCD} PDFs

Table XVIII lists the systematic uncertainties on the PDFs of E_{NCD} . The modified E_{NCD} , E'_{NCD} , was obtained from

$$E'_{\text{NCD}} = (1 + a_1^{E_{\text{NCD}}})E_{\text{NCD}}. \quad (\text{C18})$$

For each event in the PDF one hundred random numbers drawn from a Gaussian centered at zero with a width of $b_0^{E_{\text{NCD}}} E_{\text{NCD}}$ were used to construct a new PDF.

6. Background constraints

Table XIX gives the constraints on the backgrounds in Phases I and II. Table XX gives the constraints on the backgrounds in Phase III.

7. PMT background PDF

Table XXI shows the constraints on the analytical PDF given by Eq. (10) in Sec. III C for PMT background events.

8. Neutron detection efficiencies

Table XXII shows the constraints on the neutron detection efficiencies. NC interactions observed with the PMT array in Phases I and II were weighted by

$$1 + \epsilon_n^{\text{PMT}} + \epsilon_{n,\text{corr.}}^{\text{PMT}}. \quad (\text{C19})$$

NC interactions observed with the PMT array in Phase III were weighted by

$$1 + \epsilon_n^{\text{PMT}}. \quad (\text{C20})$$

NC interactions observed with the NCD array in Phase III were weighted by

$$1 + \epsilon_n^{\text{NCD}}. \quad (\text{C21})$$

TABLE XIX. Background constraints in Phases I and II. The constraints were all applied to the combined day + night value.

Background	Phase	Constraint	Fit value		Application
			Day	Night	
Internal ^{214}Bi [mBq]	I	126^{+42}_{-25}	$64.9^{+7.2}_{-7.1}$	$96.1^{+6.9}_{-6.9}$	floated
Internal ^{208}Tl [mBq]	I	$3.1^{+1.4}_{-1.3}$	$1.11^{+0.37}_{-0.36}$	$1.09^{+0.35}_{-0.34}$	floated
External ^{214}Bi [Bq]	I	6.50 ± 1.11	$11.9^{+4.2}_{-4.2}$	$2.9^{+3.3}_{-3.4}$	floated
External ^{208}Tl [Bq]	I	$0.190^{+0.063}_{-0.054}$	$0.153^{+0.202}_{-0.199}$	$0.265^{+0.157}_{-0.157}$	floated
PMT [Arb.]	I	N/A	$0.938^{+0.072}_{-0.071}$	$1.018^{+0.059}_{-0.058}$	floated
AV surface neutrons [Arb.]	I	N/A	$3.026^{+1.499}_{-1.477}$	^a	floated
AV ^{214}Bi [Arb.]	I	N/A	$2.522^{+2.252}_{-2.164}$	^a	floated
AV ^{208}Tl [Arb.]	I	N/A	$6.196^{+1.318}_{-1.315}$	^a	floated
<i>hep</i> neutrino [events]	I	15^b	N/A	N/A	fixed
Other <i>n</i> [events]	I	3.2 ± 0.8^c	N/A	N/A	shift-and-refit
Atmospheric ν [events]	I	21.3 ± 4.0	N/A	N/A	shift-and-refit
AV instrumental background [events]	I	$0.00^{+24.49d}_{-0}$	N/A	N/A	shift-and-refit
Internal ^{214}Bi [Arb.]	II	N/A	$0.742^{+0.074}_{-0.074}$	$0.495^{+0.067}_{-0.067}$	floated
Internal ^{208}Tl [mBq]	II	$2.6^{+1.2}_{-1.5}$	$0.69^{+1.68}_{-1.68}$	$1.49^{+1.41}_{-1.41}$	floated
Internal ^{24}Na [mBq]	II	0.245 ± 0.060	$0.274^{+0.342}_{-0.342}$	$0.193^{+0.284}_{-0.285}$	floated
External ^{214}Bi [Bq]	II	4.36 ± 1.05	$4.56^{+3.38}_{-3.35}$	$5.15^{+2.83}_{-2.86}$	floated
External ^{208}Tl [Bq]	II	0.129 ± 0.040	$0.216^{+0.159}_{-0.160}$	$0.071^{+0.135}_{-0.133}$	floated
PMT [Arb.]	II	N/A	$1.093^{+0.053}_{-0.053}$	$1.244^{+0.049}_{-0.049}$	floated
AV surface neutrons [Arb.]	II	N/A	$-0.359^{+0.473}_{-0.468}$	^a	floated
AV ^{214}Bi [Arb.]	II	N/A	$0.821^{+1.486}_{-1.439}$	^a	floated
AV ^{208}Tl [Arb.]	II	N/A	$6.218^{+0.981}_{-0.979}$	^a	floated
<i>hep</i> neutrino [events]	II	33^b	N/A	N/A	fixed
Other <i>n</i> [events]	II	12.0 ± 3.1^c	N/A	N/A	shift-and-refit
Atmospheric ν [events]	II	29.8 ± 5.7	N/A	N/A	shift-and-refit
AV instrumental background [events]	II	$0.00^{+36.19d}_{-0}$	N/A	N/A	shift-and-refit

^aThe fit was performed with day+night combined, so there is only one fit value for both.^bFixed at CC = 0.35 SSM, ES = 0.47 SSM, NC = 1.0 SSM [22].^cCorrelation 1.^dOne-sided, effect is symmetrized.

TABLE XX. Background constraints in Phase III. The constraints were applied on the number of events observed in the NCD array. The number of events observed in the PMT array were obtained from the number of events in the NCD array multiplied by the PMT array ratio.

Background	NCD Array		PMT Array ratio	D/N asymmetry	
	Constraint	Fit value		Constraint	Fit value
External + AV	40.9 ± 20.6	38.1 ± 19.2	0.5037	-0.020 ± 0.011	-0.019 ± 0.011
Internal	31.0 ± 4.7	30.9 ± 4.8	0.2677	-0.034 ± 0.112	-0.034 ± 0.112
NCD bulk ^a	27.6 ± 11.0	27.2 ± 9.4	0.1667	0	N/A
K2 hotspot	32.8 ± 5.3	32.6 ± 5.2	0.2854	0	N/A
K5 hotspot	$45.5^{+7.5}_{-8.4}$	$45.4^{+7.5}_{-8.3}$	0.2650	0	N/A
NCD array cables ^a	8.0 ± 5.2		0.1407	0	N/A
Atmospheric ν and cosmogenic muons	13.6 ± 2.7	13.4 ± 2.7	1.8134	0	N/A

^aIn the previous analysis of data from Phase III [8] these two backgrounds were combined.

TABLE XXI. PMT background PDF parameters for the analytical PDF given by Eq. (10) in Sec. III C.

Parameter	Phase	Day/Night	Constraint	Fit value	Application
ϵ	I	day	-6.73 ± 1.29	$-6.30^{+0.35}_{-0.56}$	scanned
ϵ	I	night	-5.64 ± 1.02	$-6.40^{+0.31}_{-0.46}$	scanned
ϵ	II	day	-6.26 ± 0.91	$-6.78^{+0.29}_{-0.37}$	scanned
ϵ	II	night	-6.98 ± 0.91	$-6.72^{+0.24}_{-0.33}$	scanned
η_1^a	I	day	0 ± 1	$-0.74^{+1.10}_{-0.54}$	scanned
η_1^b	I	night	0 ± 1	$-0.39^{+0.39}_{-0.12}$	scanned
η_1^c	II	day	0 ± 1	$0.74^{+0.42}_{-0.26}$	scanned
η_1^d	II	night	0 ± 1	$0.31^{+0.26}_{-0.13}$	scanned
η_2^a	I	day	0 ± 1	$0.09^{+0.62}_{-0.61}$	scanned
η_2^b	I	night	0 ± 1	$0.08^{+0.77}_{-0.78}$	scanned
η_2^c	II	day	0 ± 1	$-2.42^{+0.91}_{-0.39}$	scanned
η_2^d	II	night	0 ± 1	$-3.73^{+0.47}_{-0.49}$	scanned
ω_0	I	day	0.533 ± 0.014	$0.5351^{+0.0090}_{-0.0083}$	scanned
ω_0	I	night	0.533 ± 0.014	$0.5469^{+0.0071}_{-0.0072}$	scanned
ω_0	II	day	0.511 ± 0.007	$0.5096^{+0.0055}_{-0.0047}$	scanned
ω_0	II	night	0.511 ± 0.007	$0.5119^{+0.0049}_{-0.0055}$	scanned
ω_1	I	day	0.237 ± 0.051	N/A	shift-and-refit
ω_1	I	night	0.237 ± 0.051	N/A	shift-and-refit
ω_1	II	day	0.182 ± 0.095	N/A	shift-and-refit
ω_1	II	night	0.182 ± 0.095	N/A	shift-and-refit
β_s	I	day	0.182 ± 0.011	N/A	shift-and-refit
β_s	I	night	0.182 ± 0.011	N/A	shift-and-refit
β_s	II	day	0.195 ± 0.007	N/A	shift-and-refit
β_s	II	night	0.195 ± 0.007	N/A	shift-and-refit

^a $b = -1.00 + 1.29\eta_1$, $\nu = 6.63 + 0.93(0.60\eta_1 + \sqrt{1 - 0.60^2}\eta_2)$.

^b $b = 3.27 + 12.04\eta_1$, $\nu = 6.78 + 1.52(0.96\eta_1 + \sqrt{1 - 0.96^2}\eta_2)$.

^c $b = -0.33 + 2.08\eta_1$, $\nu = 5.32 + 1.01(0.91\eta_1 + \sqrt{1 - 0.91^2}\eta_2)$.

^d $b = 0.49 + 3.02\eta_1$, $\nu = 5.66 + 1.07(0.94\eta_1 + \sqrt{1 - 0.94^2}\eta_2)$.

Background neutrons from photodisintegration observed with the PMT array in Phases I and II were weighted by

$$(1 + \epsilon_n^{\text{PMT}} + \epsilon_{n,\text{corr.}}^{\text{PMT}})(1 + \epsilon_{\text{PD}}). \quad (\text{C22})$$

This uncertainty was already included in the rates of these backgrounds in Table XX for Phase III.

APPENDIX D: NEUTRINO SENSITIVITY

Table XXIII gives $S(E_\nu)$, the predicted spectrum of E_ν detectable by the SNO detector after including all effects such as the energy dependence of the cross sections, reaction thresholds, and analysis cuts, but not including neutrino oscillations.

TABLE XXII. Uncertainties in the neutron detection and photodisintegration backgrounds.

Parameter	Description	Phase	Constraint	Fit value	Application
ϵ_n^{PMT}	Neutron detection in the PMT array	I	0 ± 0.0187	N/A	shift-and-refit
ϵ_n^{PMT}	Neutron detection in the PMT array	II	0 ± 0.0124	N/A	shift-and-refit
$\epsilon_{n,\text{corr.}}^{\text{PMT}}$	Correlated neutron detection in the PMT array	I, II	0 ± 0.007	N/A	shift-and-refit
ϵ_n^{PMT}	Neutron detection in the PMT array	III	0 ± 0.028	-0.003 ± 0.028	float
ϵ_n^{NCD}	Neutron detection in the NCD array	III	0 ± 0.024	-0.001 ± 0.023	float
ϵ_{PD}	Photodisintegration	I, II	0 ± 0.02	N/A	shift-and-refit

TABLE XXIII. Predicted spectrum of E_ν detectable by the SNO detector after including all effects such as the energy dependence of the cross sections, reaction thresholds, and analysis cuts, but not including neutrino oscillations, $S(E_\nu)$. The number of events are for all three phases combined and assumes the BS05(OP) solar neutrino model ($\Phi_B = 5.69 \times 10^6 \text{ cm}^{-2}\text{s}^{-1}$) [22].

E_ν range [MeV]	CC		ES _e		ES _{$\mu\tau$}		E_ν range [MeV]	CC		ES _e		ES _{$\mu\tau$}	
	day	night	day	night	day	night		day	night	day	night	day	night
2.9–3.0	0.0	0.0	0.0	0.1	0.0	0.0	9.1–9.2	185.3	231.3	19.9	24.8	3.2	4.0
3.0–3.1	0.0	0.0	0.1	0.1	0.0	0.0	9.2–9.3	187.7	235.1	20.1	24.6	3.2	4.0
3.1–3.2	0.0	0.0	0.1	0.1	0.0	0.0	9.3–9.4	191.3	238.8	20.0	24.7	3.2	4.0
3.2–3.3	0.0	0.0	0.1	0.2	0.0	0.0	9.4–9.5	194.0	241.2	20.1	24.8	3.2	3.9
3.3–3.4	0.0	0.0	0.2	0.2	0.0	0.0	9.5–9.6	196.4	244.4	19.7	24.4	3.2	3.9
3.4–3.5	0.0	0.0	0.3	0.3	0.0	0.1	9.6–9.7	198.6	246.1	19.9	24.5	3.2	3.9
3.5–3.6	0.0	0.0	0.4	0.5	0.1	0.1	9.7–9.8	199.7	249.3	19.5	24.2	3.1	3.9
3.6–3.7	0.0	0.0	0.5	0.6	0.1	0.1	9.8–9.9	199.8	250.2	19.4	24.0	3.1	3.9
3.7–3.8	0.0	0.0	0.6	0.7	0.1	0.1	9.9–10.0	200.1	251.1	19.3	23.7	3.1	3.8
3.8–3.9	0.0	0.0	0.8	0.9	0.1	0.2	10.0–10.1	200.9	251.0	19.0	23.5	3.0	3.7
3.9–4.0	0.0	0.1	0.9	1.2	0.2	0.2	10.1–10.2	200.8	250.8	18.7	23.1	3.0	3.7
4.0–4.1	0.1	0.1	1.1	1.5	0.2	0.2	10.2–10.3	199.7	248.7	18.5	22.9	2.9	3.6
4.1–4.2	0.1	0.2	1.4	1.6	0.2	0.3	10.3–10.4	198.3	246.8	18.1	22.3	2.9	3.6
4.2–4.3	0.3	0.3	1.6	2.0	0.3	0.3	10.4–10.5	198.0	246.5	17.7	21.9	2.9	3.5
4.3–4.4	0.4	0.5	1.9	2.4	0.3	0.4	10.5–10.6	195.4	244.5	17.3	21.4	2.8	3.4
4.4–4.5	0.6	0.8	2.2	2.7	0.4	0.4	10.6–10.7	193.9	241.6	17.0	21.1	2.7	3.4
4.5–4.6	1.0	1.2	2.5	3.1	0.4	0.5	10.7–10.8	191.7	237.5	16.5	20.6	2.6	3.3
4.6–4.7	1.4	1.8	2.8	3.5	0.5	0.6	10.8–10.9	187.1	233.2	16.2	19.8	2.6	3.2
4.7–4.8	2.0	2.7	3.1	3.9	0.5	0.6	10.9–11.0	184.4	229.6	15.9	19.4	2.5	3.1
4.8–4.9	2.8	3.6	3.5	4.5	0.6	0.7	11.0–11.1	180.5	226.4	15.3	18.8	2.4	3.0
4.9–5.0	3.8	4.8	3.9	4.8	0.6	0.8	11.1–11.2	176.6	220.0	14.7	18.3	2.3	2.9
5.0–5.1	4.9	6.3	4.4	5.3	0.7	0.9	11.2–11.3	172.2	214.3	14.2	17.5	2.3	2.8
5.1–5.2	6.4	8.0	4.7	5.9	0.8	1.0	11.3–11.4	167.8	208.2	13.6	16.8	2.2	2.7
5.2–5.3	8.0	10.2	5.2	6.4	0.8	1.0	11.4–11.5	162.4	202.7	13.1	16.3	2.1	2.6
5.3–5.4	10.0	12.7	5.7	6.9	0.9	1.1	11.5–11.6	157.5	195.9	12.6	15.6	2.0	2.5
5.4–5.5	12.3	15.5	6.1	7.6	1.0	1.2	11.6–11.7	152.2	188.9	12.0	14.9	1.9	2.4
5.5–5.6	14.5	18.7	6.6	8.1	1.0	1.3	11.7–11.8	146.5	181.8	11.4	14.2	1.8	2.3
5.6–5.7	17.4	22.1	7.1	8.8	1.1	1.4	11.8–11.9	139.9	173.9	11.0	13.4	1.7	2.1
5.7–5.8	20.3	26.1	7.5	9.2	1.2	1.5	11.9–12.0	133.7	166.4	10.3	12.7	1.7	2.0
5.8–5.9	23.4	29.9	8.0	9.9	1.3	1.6	12.0–12.1	127.0	158.4	9.7	12.1	1.5	1.9
5.9–6.0	26.9	34.3	8.4	10.4	1.3	1.7	12.1–12.2	121.2	149.8	8.9	11.5	1.5	1.8
6.0–6.1	30.8	39.0	9.0	11.2	1.4	1.8	12.2–12.3	114.0	141.5	8.5	10.6	1.4	1.7
6.1–6.2	34.5	44.0	9.6	11.8	1.5	1.9	12.3–12.4	107.1	133.2	8.0	9.8	1.3	1.6
6.2–6.3	38.5	49.2	10.0	12.4	1.6	2.0	12.4–12.5	100.3	124.8	7.4	9.2	1.2	1.5
6.3–6.4	42.5	54.0	10.6	13.1	1.7	2.1	12.5–12.6	93.3	116.6	6.8	8.6	1.1	1.4
6.4–6.5	47.3	59.4	11.0	13.6	1.8	2.2	12.6–12.7	87.0	108.3	6.3	7.8	1.0	1.3
6.5–6.6	51.5	65.7	11.5	14.3	1.8	2.3	12.7–12.8	80.7	99.6	5.9	7.1	0.9	1.1
6.6–6.7	56.3	71.8	12.1	15.0	1.9	2.4	12.8–12.9	73.3	91.6	5.2	6.5	0.8	1.0
6.7–6.8	61.3	77.2	12.5	15.5	2.0	2.5	12.9–13.0	66.9	83.0	4.7	5.8	0.8	0.9
6.8–6.9	66.2	83.1	13.1	16.3	2.1	2.6	13.0–13.1	60.3	75.0	4.3	5.3	0.7	0.8
6.9–7.0	70.5	89.9	13.6	16.6	2.2	2.7	13.1–13.2	54.3	67.3	3.8	4.7	0.6	0.8
7.0–7.1	75.7	96.7	14.1	17.5	2.3	2.8	13.2–13.3	48.2	59.9	3.3	4.2	0.5	0.7
7.1–7.2	81.1	103.4	14.5	18.2	2.3	2.9	13.3–13.4	42.4	52.5	2.9	3.7	0.5	0.6
7.2–7.3	86.8	109.3	15.1	18.5	2.4	3.0	13.4–13.5	36.9	45.8	2.5	3.1	0.4	0.5
7.3–7.4	92.2	116.8	15.3	19.0	2.5	3.1	13.5–13.6	31.5	39.6	2.1	2.7	0.3	0.4
7.4–7.5	98.6	123.3	16.0	19.8	2.5	3.1	13.6–13.7	27.0	33.3	1.8	2.2	0.3	0.4
7.5–7.6	103.6	130.4	16.4	20.3	2.6	3.3	13.7–13.8	22.6	27.9	1.5	1.9	0.3	0.3
7.6–7.7	108.6	138.2	16.9	20.9	2.7	3.3	13.8–13.9	18.7	23.3	1.2	1.5	0.2	0.2
7.7–7.8	115.1	145.0	17.1	21.6	2.7	3.4	13.9–14.0	15.2	19.1	1.0	1.2	0.2	0.2
7.8–7.9	120.5	152.6	17.8	21.7	2.8	3.4	14.0–14.1	12.2	15.2	0.8	1.0	0.1	0.2
7.9–8.0	126.3	159.7	17.8	22.0	2.9	3.5	14.1–14.2	9.5	12.0	0.6	0.8	0.1	0.1
8.0–8.1	131.9	166.7	18.2	22.5	2.9	3.6	14.2–14.3	7.4	9.2	0.5	0.6	0.1	0.1
8.1–8.2	137.7	172.1	18.4	22.8	3.0	3.6	14.3–14.4	5.7	7.0	0.3	0.4	0.1	0.1
8.2–8.3	143.2	179.2	18.9	23.2	3.0	3.7	14.4–14.5	4.4	5.2	0.3	0.3	0.0	0.1

TABLE XXIII. (*Continued.*)

E_ν range [MeV]	CC		ES_e		$ES_{\mu\tau}$		E_ν range [MeV]	CC		ES_e		$ES_{\mu\tau}$	
	day	night	day	night	day	night		day	night	day	night	day	night
8.3–8.4	148.8	186.0	19.0	23.5	3.0	3.7	14.5–14.6	3.2	4.0	0.2	0.2	0.0	0.0
8.4–8.5	153.7	193.3	19.3	23.9	3.1	3.8	14.6–14.7	2.4	3.1	0.2	0.2	0.0	0.0
8.5–8.6	159.0	199.2	19.6	24.0	3.1	3.9	14.7–14.8	1.8	2.1	0.1	0.1	0.0	0.0
8.6–8.7	164.0	205.5	19.6	24.3	3.1	3.9	14.8–14.9	1.3	1.5	0.1	0.1	0.0	0.0
8.7–8.8	168.2	211.5	19.6	24.6	3.1	3.9	14.9–15.0	0.9	1.1	0.1	0.1	0.0	0.0
8.8–8.9	172.6	216.6	20.0	24.8	3.2	3.9	15.0–15.1	0.7	0.8	0.0	0.1	0.0	0.0
8.9–9.0	177.2	222.1	20.0	24.7	3.2	4.0	15.1–15.2	0.4	0.6	0.0	0.0	0.0	0.0
9.0–9.1	181.6	226.8	20.1	25.1	3.2	3.9	15.2–15.3	0.2	0.3	0.0	0.0	0.0	0.0

^aPresent address: Center for Astrophysics and Space Astronomy, University of Colorado, Boulder, CO.

^bPresent address: Institut für Kern- und Teilchenphysik, Technische Universität Dresden, Dresden, Germany.

^cPresent address: Department of Physics, University of California, Davis, CA.

^dPresent address: Institut für Experimentelle Kernphysik, Karlsruher Institut für Technologie, Karlsruhe, Germany.

^ePresent address: CERN, Geneva, Switzerland.

^fPresent address: Department of Physics, Hiroshima University, Hiroshima, Japan.

^gPresent address: Sanford Laboratory at Homestake, Lead, SD.

^hPresent address: Department of Physics, University of North Carolina, Chapel Hill, NC.

ⁱPresent address: Center of Cosmology and Particle Astrophysics, National Taiwan University, Taiwan.

^jPresent address: Black Hills State University, Spearfish, SD.

^kPresent address: Physics Department, Lancaster University, Lancaster, UK.

^lPresent address: Institute for Space Sciences, Freie Universität Berlin, Leibniz-Institute of Freshwater Ecology and Inland Fisheries, Germany.

^mPresent address: Department of Physics and Astronomy, University of Alabama, Tuscaloosa, AL.

ⁿPresent address: Department of Physics, University of Liverpool, Liverpool, UK.

^oPresent address: Center for Experimental Nuclear Physics and Astrophysics, and Department of Physics, University of Washington, Seattle, WA.

^pPresent address: Department of Physics, University of California, Santa Barbara, CA.

^qPresent address: Department of Physics, Royal Holloway University of London, Egham, Surrey, UK.

^rAddress after January 2012: Physics Department, University of California at Berkeley, and Lawrence Berkeley National Laboratory, Berkeley, CA.

^sPresent address: Department of Physics and Astronomy, University of Sussex, Brighton, UK.

^tPresent address: Department of Chemistry and Physics, Armstrong Atlantic State University, Savannah, GA.

^uPresent address: CEA-Saclay, DSM/IRFU/SPP, Gif-sur-Yvette, France.

^vPresent address: Department of Physics, Queen's University, Kingston, Ontario, Canada.

^wPresent address: Physics Department, McGill University, Montreal, QC, Canada.

^xPresent address: Pacific Northwest National Laboratory, Richland, WA.

^yAdditional Address: Imperial College, London, UK.

^zPresent address: Department of Physics, Queen Mary University, London, UK.

^{aa}Deceased.

^{bb}Present address: Department of Physics, Princeton University, Princeton, NJ.

[1] H. H. Chen, *Phys. Rev. Lett.* **55**, 1534 (1985).

[2] L. Wolfenstein, *Phys. Rev. D* **17**, 2369 (1978).

[3] S. Mikheyev and A. Smirnov, *Sov. J. Nucl. Phys.* **42**, 913 (1985).

[4] Z. Maki, M. Nakagawa, and S. Sakata, *Prog. Theor. Phys.* **28**, 870 (1962).

[5] B. Pontecorvo, *Sov. Phys. JETP* **7**, 172 (1958).

[6] A. M. Serenelli, S. Basu, J. W. Ferguson, and M. Asplund, *Astrophys. J. Lett.* **705**, L123 (2009).

[7] B. Aharmim *et al.* (SNO Collaboration), *Phys. Rev. C* **81**, 055504 (2010).

[8] B. Aharmim *et al.* (SNO Collaboration), *Phys. Rev. Lett.* **101**, 111301 (2008).

[9] J. Boger *et al.* (SNO Collaboration), *Nucl. Instrum. Methods Phys. Res. A* **449**, 172 (2000).

[10] G. Doucas, S. Gil, N. A. Jelly, L. McGarry, M. E. Moorhead, N. W. Tanner, and C. E. Waltham, *Nucl. Instrum. Methods Phys. Res. A* **370**, 579 (1996).

[11] B. Aharmim *et al.*, *Nucl. Instrum. Methods Phys. Res. A* **604**, 531 (2009).

[12] J. F. Amsbaugh *et al.*, *Nucl. Instrum. Methods Phys. Res. A* **579**, 1054 (2007).

[13] B. Aharmim *et al.* (SNO Collaboration), *Phys. Rev. C* **87**, 015502 (2013).

[14] B. Aharmim *et al.* (SNO Collaboration), *Phys. Rev. C* **72**, 055502 (2005).

[15] B. Aharmim *et al.* (SNO Collaboration), *Phys. Rev. D* **72**, 052010 (2005).

[16] Q. R. Ahmad *et al.* (SNO Collaboration), *Phys. Rev. Lett.* **89**, 011302 (2002).

[17] In our previous analysis of data from Phases I and II [7] we described this method as imposing a unitarity constraint, which was not technically correct.

[18] P.-L. Drouin, Ph.D. thesis, Carleton University, 2011.

- [19] T. C. Andersen *et al.*, *Nucl. Instrum. Methods Phys. Res. A* **501**, 386 (2003).
- [20] T. C. Andersen *et al.*, *Nucl. Instrum. Methods Phys. Res. A* **501**, 399 (2003).
- [21] H. O’Keeffe, T. Burritt, B. Cleveland, G. Doucas, N. Gagnon *et al.*, *Nucl. Instrum. Methods Phys. Res. A* **659**, 182 (2011).
- [22] J. N. Bahcall, A. M. Serenelli, and S. Basu, *Astrophys. J. Lett.* **621**, L85 (2005).
- [23] M. R. Dragowsky *et al.*, *Nucl. Instrum. Methods Phys. Res. A* **481**, 284 (2002).
- [24] A. W. P. Poon, R. J. Komar, C. E. Waltham, M. C. Browne, R. G. H. Robertson, N. P. Kherani, and H. B. Mak, *Nucl. Instrum. Methods Phys. Res. A* **452**, 115 (2000).
- [25] N. J. Tagg, A. S. Hamer, B. Sur, E. D. Earle, R. L. Helmer, G. Jonkmans, B. A. Moffat, and J. J. Simpson, *Nucl. Instrum. Methods Phys. Res. A* **489**, 178 (2002).
- [26] K. Boudjemline *et al.*, *Nucl. Instrum. Methods Phys. Res. A* **620**, 171 (2010).
- [27] W. T. Winter, S. J. Freedman, K. E. Rehm, and J. P. Schiffer, *Phys. Rev. C* **73**, 025503 (2006).
- [28] F. James and M. Roos, *Comput. Phys. Commun.* **10**, 343 (1975).
- [29] S. Habib, Ph.D. thesis, University of Alberta, 2011.
- [30] R. A. Ott, Ph.D. thesis, Massachusetts Institute of Technology, 2011.
- [31] B. Beltran *et al.*, *New J. Phys.* **13**, 073006 (2011).
- [32] N. S. Oblath, Ph.D. thesis, University of Washington, 2009.
- [33] R. Martin, Ph.D. thesis, Queen’s University, 2009.
- [34] A. J. Wright, Ph.D. thesis, Queen’s University, 2009.
- [35] N. Barros, Ph.D. thesis, University of Lisbon, 2011.
- [36] T. Schwetz, M. Tórtola, and J. W. F. Valle, *New J. Phys.* **13**, 063004 (2011).
- [37] <http://www.sns.ias.edu/~jnb/SNdata/sndata.html>.
- [38] A. M. Dziewonski and D. L. Anderson, *Phys. Earth Planet. Inter.* **25**, 297 (1981).
- [39] A. M. Dziewonski, A. L. Hales, and E. R. Lapwood, *Phys. Earth Planet. Inter.* **10**, 12 (1975).
- [40] J. N. Abdurashitov *et al.* (SAGE Collaboration), *Phys. Rev. C* **80**, 015807 (2009), contains combined analysis with the following references; M. Altmann *et al.* (GNO Collaboration), *Phys. Lett. B* **616**, 174 (2005); F. Kaether, Ph.D. thesis, Heidelberg, 2007.
- [41] B. T. Cleveland *et al.*, *Astrophys. J.* **496**, 505 (1998).
- [42] G. Bellini *et al.* (Borexino Collaboration), *Phys. Rev. Lett.* **107**, 141302 (2011).
- [43] G. Bellini *et al.* (Borexino Collaboration), *Phys. Rev. D* **82**, 033006 (2010).
- [44] J. Hosaka *et al.* (Super-Kamiokande Collaboration), *Phys. Rev. D* **73**, 112001 (2006).
- [45] J. P. Cravens *et al.* (Super-Kamiokande Collaboration), *Phys. Rev. D* **78**, 032002 (2008).
- [46] K. Abe *et al.* (Super-Kamiokande Collaboration), *Phys. Rev. D* **83**, 052010 (2011).
- [47] G. Bellini *et al.* (Borexino Collaboration), *Phys. Lett. B* **707**, 22 (2012).
- [48] S. Abe *et al.* (KamLAND Collaboration), *Phys. Rev. C* **84**, 035804 (2011).
- [49] A. Gando *et al.* (KamLAND Collaboration), *Phys. Rev. D* **83**, 052002 (2011).
- [50] T. A. Mueller *et al.*, *Phys. Rev. C* **83**, 054615 (2011).
- [51] G. L. Fogli, E. Lisi, A. Marrone, A. Palazzo, and A. M. Rotunno, *Phys. Rev. D* **84**, 053007 (2011).
- [52] F. P. An *et al.*, *Chinese Physics C* **37**, 011001 (2013).
- [53] J. K. Ahn *et al.* (RENO Collaboration), *Phys. Rev. Lett.* **108**, 191802 (2012).
- [54] Y. Abe *et al.* (Double Chooz Collaboration), *Phys. Rev. Lett.* **108**, 131801 (2012).
- [55] K. Abe *et al.* (T2K Collaboration), *Phys. Rev. Lett.* **107**, 041801 (2011).
- [56] P. Adamson *et al.* (MINOS Collaboration), *Phys. Rev. Lett.* **107**, 181802 (2011).
- [57] M. Apollonio *et al.*, *Eur. Phys. J. C* **27**, 331 (2003).